UNDERSTANDING THE COMPLEX INTERPLAY OF FACTORS IN RAIL BUCKLING: A FINITE ELEMENT APPROACH

A Dissertation

by

TING-MING LIU

Submitted to the Graduate and Professional School of
Texas A&M University
in partial fulfillment of the requirements for the degree of

DOCTOR OF PHILOSOPHY

Chair of Committee,	David H. Allen
Committee Members,	HeonYong Kang
	James G. Boyd
	Yong-Rak Kim
Head of Department,	Sharath Girimaji

May 2025

Major Subject: Ocean Engineering

ABSTRACT

Due to its complexity, rail buckling is a mathematically nonlinear phenomenon affected by a wide range of service conditions, including but not limited to field temperature, track geometry, tie-ballast interactions, material properties of the structural components, train-induced lift-off, and different types of boundary conditions. Although several research studies have focused on this issue, it is still challenging to model this problem efficiently while maintaining both simplicity and accuracy. In this research, a finite element (FE) computer code based on the Euler-Bernoulli beam theory is developed to account for all the above phenomena, thereby resulting in a Python-based FE program that only requires a few minutes of runtime to complete one rail buckling simulation.

Building on the previous work by Musu, Allen, and Fry, this study extends the model's development by including the displacement-control based solving algorithm, as well as modifying the tie-ballast interface resistance formulation, and restructuring the variational formulation of the governing differential equations.

The key focus of this research is to demonstrate the application of the displacement-control algorithm for modeling rail buckling problems. Additionally, the study analyzes the impact of initial rail misalignments on buckling behavior. A nonlinear tie-ballast resistance formulation is incorporated into the model to replicate single-tie push test (STPT) experimental outputs, enhancing the realism of the results. The findings indicate that an increase in misalignment or a decrease in the maximum lateral tie-ballast resistance value significantly reduces the critical rail buckling load, highlighting these factors as crucial in predicting rail buckling.

ACKNOWLEDGEMENTS

I would like to thank my PhD advisor, Dr. Allen, for his invaluable guidance and support throughout my doctoral journey. I also extend my sincere appreciation to my committee members, Dr. Kim, Dr. Boyd, and Dr. Kang, as well as researcher Dr. Steven Wilk at MxV Rail, for their thoughtful feedback and encouragement that helped shape my research.

I am grateful to my labmates and friends, especially Gavin Whetstone, Valentina Musu, and Pratiwi Fudlailah, whose support made the challenging four years of my PhD more manageable. Without their encouragement, I wouldn’t have been able to complete this journey.

Finally, I want to express my heartfelt thanks to all my friends and family for their unwavering support and belief in me.

CONTRIBUTORS AND FUNDING SOURCES

Contributors

This research builds upon the foundational work of Dr. David H. Allen and Dr. Valentina Musu. Their pioneering efforts provided the groundwork upon which this study expands, furthering the understanding of the topic and addressing new challenges.

Building on their work, the author conducted all further analyses and completed the remaining work independently.

Funding Sources

This research was supported by funding from the U.S. Department of Transportation (USDOT) through the University Transportation Center for Railway Safety under Grant Number 69A3552348340. Additional funding was provided by MxV Rail, whose support was instrumental in advancing the project's practical applications. This financial support enabled the successful completion of the study and the dissemination of its findings. The content is solely the responsibility of the author and does not necessarily represent the official views of the awarding offices. The author is deeply grateful for the funding and resources provided by these organizations, without which this work would not have been possible.

NOMENCLATURE

A	Cross-sectional area of the rail
DOF	Degrees of freedom
d_{mis}	Misalignment value
d_{tie}	Tie-spacing
E	Young's modulus of the rail
FEM	Finite Element Method
FRA	Federal Railroad Administration
$\boldsymbol{F}$	Force vector of the global system
$\boldsymbol{F^e}$	Force vector of element e
F_x	Longitudinal tie-ballast resistance
F_y	Lateral tie-ballast resistance
$F_{y,lt}$	Limit lateral tie-ballast resistance
$F_{y,pk}$	Peak lateral tie-ballast resistance
f_x	Longitudinal tie-ballast resistance per unit length
f_y	Lateral tie-ballast resistance per unit length
$\boldsymbol{I^e}$	Finite element system functional matrix of element e
I_{yy}	Moment of inertia of the rail about the y-axis
I_{zz}	Moment of inertia of the rail about the z-axis
$\boldsymbol{K}$	Stiffness matrix of the global system
$\boldsymbol{K^e}$	Stiffness matrix of element e

k_z	Track modulus of the rail ballast system
L	Buckled region length of the rail
L^e	Generic element length in the discretized domain
M_y	Resultant moment about the y-axis
M_z	Resultant moment about the z-axis
m_z	Fastener rotational resistance per unit length
N	Vertical normal load value
N_{STPT}	Vertical normal load value during the STPT
N_{tie}	Weight of one single tie
n_{rail}	Rail weight per unit length
P	Axial force resultant along the x-axis
P^T	Thermally induced axial force resultant along the x-axis
P_{cr}	Critical buckling load
P_{min}	Minimum buckling load
p_x	Externally applied distributed force per unit length along the x-axis
p_y	Externally applied distributed force per unit length along the y-axis
p_z	Externally applied distributed force per unit length along the z-axis
$\boldsymbol{q}$	Displacement vector of the global system
$\boldsymbol{q}^{\boldsymbol{e}}$	Displacement vector of element e
$\boldsymbol{R}^{\boldsymbol{m}}$	Force residual vector at iteration m
RNT	Rail neutral temperature
S	Fastener rotational stiffness

STPT	Single-tie push test
t	Time
u	Displacement of the rail's centroid along the x-axis (or analogous tie longitudinal displacements measured during STPT testing)
u_i^e	Axial displacement component at the i-th end of element e
V_y	Lateral force resultant along the y-axis
V_z	Vertical force resultant along the z-axis
v	Displacement of the rail's centroid along the y-axis (or analogous tie lateral displacements measured during STPT testing)
v_i^e	Lateral displacement component at the i-th end of element e
v_{lt}	Limit Lateral Tie-Ballast displacement
v_{pk}	Peak Lateral Tie-Ballast Displacement
w	Displacement of the rail's centroid along the z-axis
w_i^e	Vertical displacement component at the i-th end of element e
x	Coordinate axis along the longitudinal direction of the rail
y	Coordinate axis along the vertical direction of the rail
$\bar{y}$	Horizontal distance from the centroid
z	Coordinate axis along the vertical direction of the rail
$\bar{z}$	Vertical distance from the centroid
z^*	Vertical distance between the centroid and the rail bottom
α	Coefficient of thermal expansion of the rail
ΔT	Temperature change from the rail neutral temperature

ε_{xx}	Axial strain within the rail
λ_i	Tie-ballast resistance scaling factor of the i direction
μ	Coefficient of friction at the tie-ballast interface
μ_{STPT}	Coefficient of friction at the tie-ballast interface during the STPT
θ_y	Rotation of the rail's neutral surface about the y-axis
$\theta_{y,i}^e$	Rotation component about the y-axis at the i-th end of element e
θ_z	Rotation of the rail's neutral surface about the z-axis
$\theta_{z,i}^e$	Rotation component about the z-axis at the i-th end of element e
σ_{xx}	Axial stress within the rail
T_z	Fastener rotational resistance
τ_y	Distributed moment in the x-z plane caused by longitudinal tie-ballast resistance
τ_z	Fastener rotational resistance per unit length
ξ_n	Hermitian shape function of the axial displacements
η_n	Hermitian shape function of the lateral displacements
ζ_n	Hermitian shape function of the vertical displacements

TABLE OF CONTENTS

Page

LIST OF FIGURES

Page

LIST OF TABLES

CHAPTER I

INTRODUCTION

Rail buckling is a catastrophic event that can cause serious safety issues in the rail industry. According to studies (Federal Railroad Administration, 2024), around 11% of the total railroad accidents within the 2021 to 2023 could be related to buckling. These accidents can result in billions of dollars lost and even lead to human casualties. However, today, there are still no clear guidelines for protecting against rail buckling.

Figure 1 Photograph showing thermally induced buckling of a railway (reprinted with permission from ABproTWE, CC BY-SA 3.0, via Wikimedia Commons)

Buckling is a type of structural instability oftentimes induced by thermal effects in the rail industry. Railroad engineers note that buckling usually happens in summer and during the day when the ambient temperature is high, and it is often referred to as a “sun kink”. Notable examples include the 2002 Amtrak Auto Train derailment in Florida, which resulted in multiple fatalities due to heat-induced rail buckling (National Transportation Safety Board, 2003), and the derailment of the Amtrak Capitol Limited in Maryland the same year, caused by similar conditions (National Transportation Safety Board, 2004). These incidents underscore the importance of addressing this issue comprehensively. However, field observations also show that rail misalignments (track-walk), broken fasteners (spikes), weak tie-ballast resistance performance, and other imperfections could also affect whether a rail would buckle or not. Even though modern commercial finite element software can model this problem, the expense, the training needed, and the necessary computation time obviate deployment of commercially available codes in the field. Accordingly, an efficient method, which nonetheless includes a minimum level of complexity, needs to be developed to prevent rail buckling.

The body of literature on this subject is extensive. In the 18th century, the first concise beam-bending model was reported (Euler, 1744). Two centuries later, Timoshenko applied this procedure to predict deformations of railroad structures (Timoshenko, 1915, 1927). Though not specific to rails, the vertical deformation of a beam on an elastic foundation has also been investigated (Oden, 1967), providing an analytic solution to estimate how rails can deform vertically under train load.

More recently, Kerr formulated a detailed rail-response-predicting model utilizing beam theory (Kerr, 1974; Kerr et al., 1976), and soon thereafter, the rail buckling problem started to gain more attention. A finite element model deploying the previously mentioned formulation was used to analyze the relation between buckling temperature, initial lateral imperfections, and elastic-plastic type ballast resistance (Tvergaard and Needleman, 1981). Lift-off problems and wheel-track interaction were also examined, revealing that vehicle speed and axle load are crucial factors influencing wheel-rail impact loads (Dong et al., 1994). A series of experimental and numerical studies on the stability of continuously welded rail (CWR) and thermal buckling led to significant advancements in this field, including the development of Fourier analysis models that incorporate vehicle loads or operate without them (Kish et al., 1982, 1985; Kish and Samavedam, 1991, 2013). Research indicates that vertical displacements impact rail buckling, highlighting that describing the problem as 2D may be an oversimplification (Lim et al., 2003). Post-buckling analyses conducted using shooting techniques concluded that lateral tie-ballast resistance plays a more dominant role compared to longitudinal tie-ballast resistance (Li and Batra, 2007; Yang and Bradford, 2016).

As it is gaining popularity, commercial finite element software is used to analyze rail buckling problems (Pucillo, 2016; Miri et al., 2021). However, some shortcomings of current solving procedures, such as solving an overly simplified boundary value problem, extended runtime, operating difficulty, and limited flexibility, must be resolved to provide practical and prompt support to railroad safety inspectors.

With these objectives in mind, this research develops a finite element computational algorithm designed to deliver readily accessible yet accurate predictions of rail buckling under a wide range of environmental factors. Building on the work of Musu (2023), which emphasized lift-off effects, the updated model incorporates displacement control into the nonlinear solving procedure. This enhancement not only significantly improves computational efficiency but also facilitates accurate post-buckling analysis and provides deeper insights into the system's response. Additionally, the model updates several nonlinear effect formulations to better reflect real-world conditions and integrates practical input parameters, including but not limited to, initial rail misalignment, rail weight, tie-spacing, and tie-ballast interface friction coefficient. A comprehensive sensitivity study has been conducted to evaluate the significance of these parameters. Capable of generating results within minutes on a standard Intel i7 laptop, this efficient and versatile tool provides a practical and accessible solution for advancing rail safety.

CHAPTER II

MODEL DEVELOPMENT

This section outlines the assumptions underlying the development of the model used in this research, which is based on thermoelastic Euler-Bernoulli beam theory. Unlike the typical formulation, this model incorporates large strain effects and additional influences such as nonlinear tie-ballast resistance to enhance its accuracy and applicability for rail applications.

Overview of the Track Structure

As illustrated in Figure 2, the rail is affixed to the crossties using fasteners (spikes). The ballast, composed of crushed stone aggregate, is deposited on the rail bed beneath the ties (sleepers), which are typically embedded within it. In some rail systems, tie plates may clip onto the sides of the ties, enhancing the rigidity of the structure, but their effects will not be analyzed separately and will instead be incorporated into the tie-ballast interaction within this research. Note that the coordinate axes x, y, and z correspond to the axial (longitudinal), lateral, and vertical directions relative to the direction of travel.

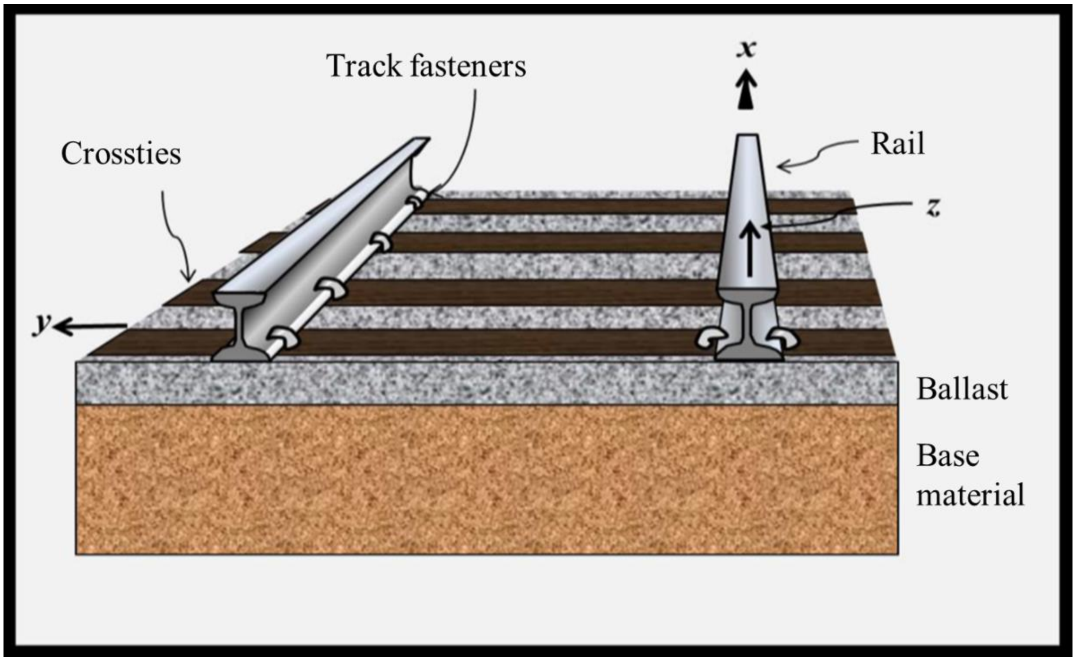

Figure 2 Generic rail with right-handed coordinate system as shown (reprinted with Permission from Allen and Fry, 2017)

Effects on the Track

Tie-Ballast Resistance

The ties attached to the rail provide resistance to help prevent the rail from deforming, and research has shown that this can be a highly nonlinear effect (Samavedam et al., 1995).

For lateral resistance (F_y), this research has deployed the results of single-tie push tests (STPT) (Wilk, 2024). STPTs are experiments that apply a lateral load to a single tie embedded within the track structure to measure the force-displacement relationship, as depicted in Figure 3. A load cell is connected to the tie, and as it pushes away from a fixed location, the lateral displacement of the tie (v) is measured.

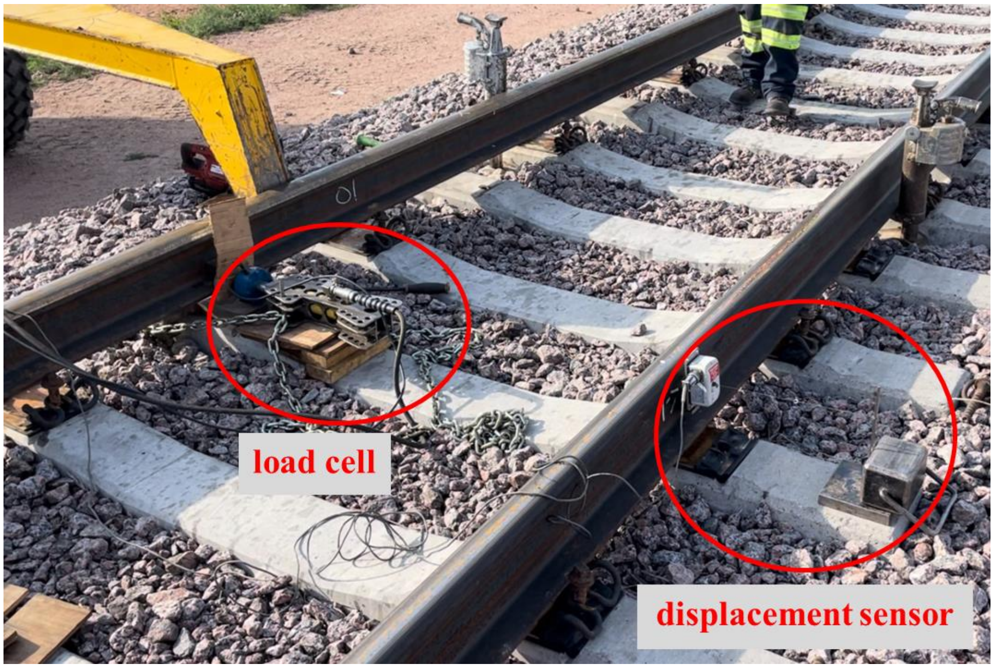

Figure 3 Photograph showing the operation of a single-tie push test experiment conducted by MxV Rail, Pueblo, CO

Although the tie is disconnected from the original track, it remains embedded in the ballast, meaning the measured resistance arises solely from the tie-ballast interaction. As the relationship between F_y and v can be highly nonlinear, it is generally categorized based on the ballast condition.

In the first case, known as the disturbed condition, the track has been recently tamped. Tamping, a process used to align and level the track, inevitably disrupts and loosens the ballast structure. This disturbance results in a force-displacement relationship that can typically be represented by a bilinear curve, characterized by an initially stiff slope indicating high resistance to small displacements, which eventually levels off to a constant value as v increases.

In the second case, referred to as the compacted condition, the track system has undergone sufficient usage, leading to ballast consolidation. Over time, the ballast aggregates interlock with one another, resulting in a higher peak resistance value. The force-displacement relationship in this condition can typically be represented by a trilinear curve. Initially, F_y increases linearly with v, reflecting the high stiffness of the interlocked ballast. Once the peak resistance is reached, F_y gradually decreases at a steady rate before stabilizing at a negligible value as v continues to increase.

The mathematical curve-fitting formulations for the two different conditions are expressed as follows:

- Disturbed condition (bilinear formulation):

$$F_y(v) = \begin{cases} \frac{F_{y,lt}}{v_{lt}} \cdot |v| \cdot \mathrm{sgn}(-v), & |v| \le v_{lt} \\ F_{y,lt} \cdot \mathrm{sgn}(-v), & |v| > v_{lt} \end{cases} \tag{1}$$

Here, $F_{y,lt}$ represents the constant limit force, and v_{lt} denotes the corresponding lateral displacement.

- Compacted condition (trilinear formulation):

$$F_y(v) = \begin{cases} \frac{F_{y,pk}}{v_{pk}} \cdot |v| \cdot \mathrm{sgn}(-v), & |v| \le v_{pk} \\ \left[F_{y,pk} + \frac{F_{y,lt} - F_{y,pk}}{v_{lt} - v_{pk}} \cdot \left(|v| - v_{pk}\right)\right] \cdot \mathrm{sgn}(-v), & v_{pk} < |v| \le v_{lt} \\ F_{y,lt} \cdot \mathrm{sgn}(-v), & |v| > v_{lt} \end{cases} \tag{2}$$

The term $F_{y,pk}$ represents the peak force, and v_{pk} denotes the corresponding lateral displacement. Additionally, the force directions are defined to oppose the displacement directions. Therefore, the magnitude values are multiplied by $\mathrm{sgn}(-v)$ to represent the correct direction. It is worth noting that Equation (2) becomes identical to Equation (1) when $F_{y,lt} = F_{y,pk}$. As a result, the disturbed condition can be regarded as a simplified version of the compacted formulation.

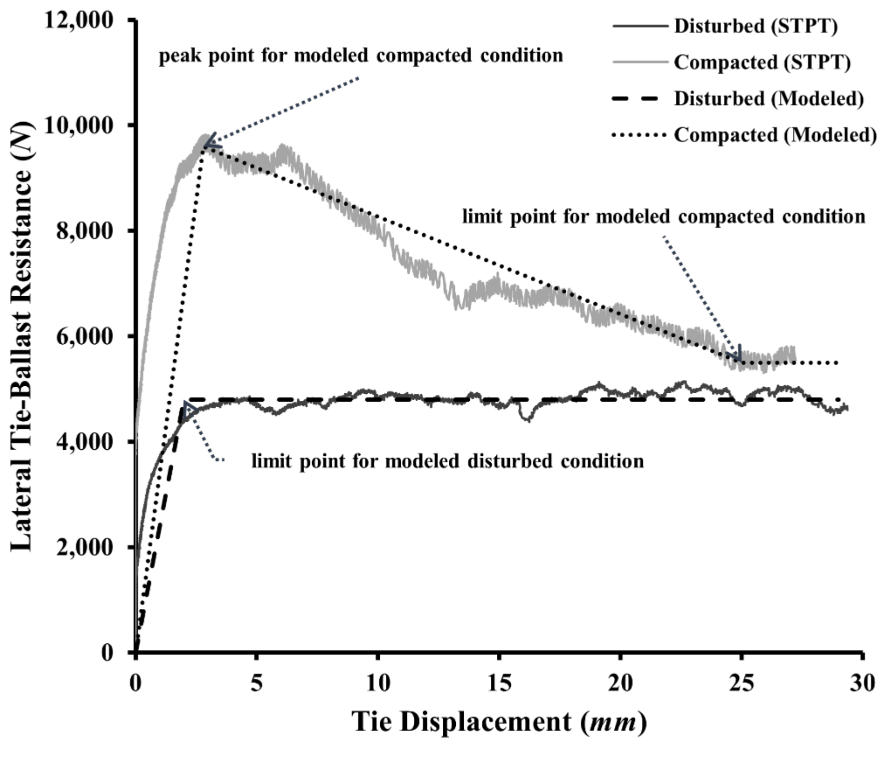

Figure 4 Demonstration of actual STPT experiment results alongside the corresponding curve-fitting model for the displacement-resistance relationship

The behaviors of both cases are illustrated together in Figure 4, where the bilinear and trilinear curves demonstrate the differences between the disturbed and compacted condition. Note that the force-resistance relationship shown in the graph represents magnitude values only, and the direction of the force relative to displacement is not depicted.

The relation between longitudinal resistance (F_x) and axial displacement (u) can be measured with a similar procedure. While previous research has shown that the F_x-u relationship is inherently nonlinear (Tvergaard and Needleman, 1981; Nobakht et al., 2022), the precise mechanism governing this type of load has not yet been determined. For simplicity, F_x is assumed to vary linearly with u in this study, as illustrated below:

$$F_x(u) = -k_x \cdot u \tag{3}$$

Here, k_x is the longitudinal tie-ballast resistance coefficient and is independent of u.

Before incorporating Equation (1) and (2) into the model, certain calibrations and modifications must be performed. F_y comprises three major components (Li et al., 1997): the friction between the bottom of the ties and the ballast, the friction between the sides of the ties and the ballast, and the resistance of the ballast shoulder to lateral displacement, as shown in Figure 5. A similar approach applies to F_x.

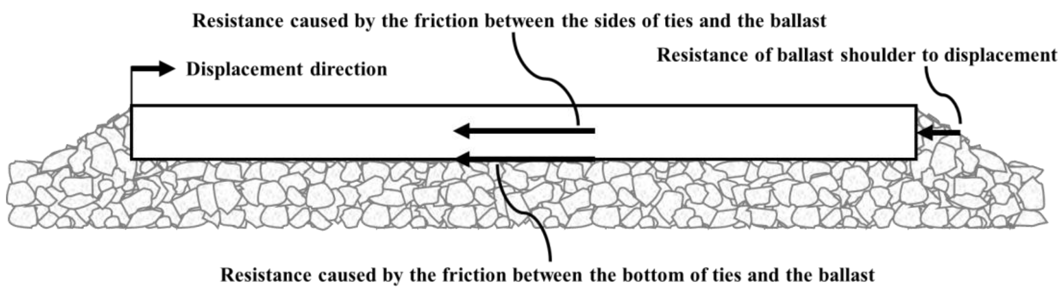

Figure 5 Illustration of the tie-ballast interaction, showing the three major lateral resistance components

To ensure the applicability of the STPT experimental results across different tie weights, loading conditions, and friction coefficients (μ) associated with tie materials or surface conditions, modifications are required. The values of μ are assumed to be known a priori for both the STPT experiment and the modeled scenario. As vertical loads (N)—such as those caused by tie weight or train loads—increase, it is assumed that the bottom friction changes proportionally, while the changes of the side friction and ballast shoulder resistance remain negligible.

Based on these assumptions, Coulomb's friction law is used to determine a scaling factor (λ) for the tie-ballast resistance curve:

$$\lambda_i = \frac{F_i + \mu \cdot N - \mu_{STPT} \cdot N_{STPT}}{F_i} \tag{4}$$

Where subscripts i denote the corresponding direction (longitudinal or lateral), and subscripts $STPT$ represent the values specific to the STPT experiments. λ_i must be calculated for each scenario and applied to modify the original tie-ballast resistance curve before simulation.

In addition, the two resistances could be considered as point loads acting on the track. To facilitate model construction, the load values are divided by tie-spacing, and the final forms of the resistances are treated as distributive loads along the track, as shown below:

$$f_x(u) = \frac{\lambda_x \cdot F_x}{d_{tie}} \tag{5}$$

$$f_y(v) = \frac{\lambda_y \cdot F_y}{d_{tie}} \tag{6}$$

Terms f_x and f_y represents the tie-ballast resistance per unit length in the corresponding longitudinal and lateral directions, respectively, and d_{tie} denotes the tie-spacing of the track system.

Vertical Support of the Ballast

Contrary to the x and y directions, friction is assumed to be negligible in the z direction. Nonetheless, the vertical support of the foundation (ballast) (f_z) is assumed to be a linear function of the vertical displacements (w) and can be expressed as:

$$f_z(w) = -k_z \cdot w \tag{7}$$

Where f_z has units of force per unit length, and k_z represents the track modulus, which is assumed to be constant and can be acquired from experimental data (Oden, 1967).

Fastener Rotational Resistance

Fasteners are used to connect rails and ties, which can provide rotational resistance to prevent the rail from bending, as shown in Figure 6. Similar to F_x, the exact relationship between the rotation angle (θ_z) and the rotational resistance (T_z) provided by the fastener remains unclear. Additionally, this relationship may be nonlinear and highly dependent on the type of fastener used (Samavedam et al., 1993). In this study, however, T_z is assumed to vary linearly with θ_z, proportional to the rotational stiffness (S), which is treated as a constant, as shown in Equation (8).

$$\mathrm{T}_z(\theta_z) = -S \cdot \theta_z \tag{8}$$

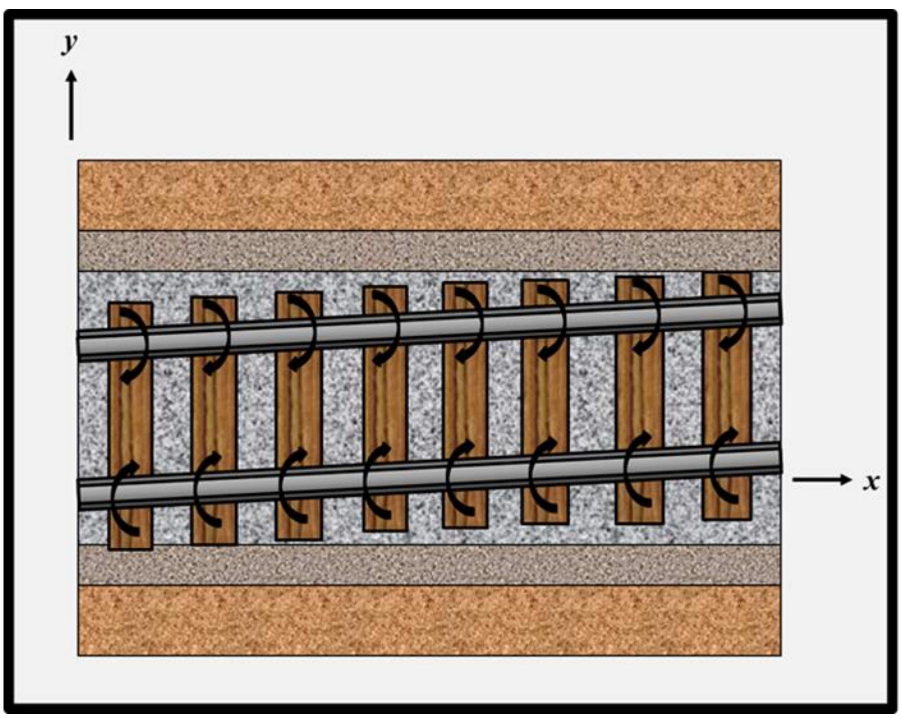

Figure 6 Demonstration of the rotational resistance induced by fasteners and ties (reprinted with permission from Allen and Fry, 2017)

In addition, T_z is converted from a point moment formulation into a distributed moment formulation by dividing the equation by d_{tie}. Similar to the approach used for tie-ballast resistance, this conversion simplifies its application to the model and expresses it in units of moment per unit length (τ_z), as shown below:

$$\tau_z(\theta_z) = \frac{\mathrm{T}_z}{d_{tie}} \tag{9}$$

Thermal Effects

Rail buckling is often induced by thermal effects, including high ambient temperature, direct sunlight, and/or frictional heating caused by vehicle operation. Thus, the thermal stresses caused by thermal expansion must be taken into consideration. Throughout this research, heat transfer effects will be neglected, and it is assumed that the rail temperature changes evenly, without any local variations. A linear thermoelastic constitutive equation is deployed within this model, given by:

$$\sigma_{xx} = E(\varepsilon_{xx} - \alpha \cdot \Delta T) \tag{10}$$

Where E is the Young's modulus, ε_{xx} is the axial strain, α represents the coefficient of thermal expansion, and ΔT is the current temperature difference compared to the rail neutral temperature (RNT), implying that at RNT there will be no thermal stress applied to the system.

Finally, other sources of loads or moments applied to the track, such as vehicle loads, could be described as distributed loads or concentrated point loads applied to the beam. The means by which these additional external loadings could affect rail buckling will be discussed in later sections.

Boundary Value Problem

As the rail is slender, and the axial dimension is much greater than the lateral and vertical dimensions, the Euler-Bernoulli assumption is applied to this model, meaning that cross-sections of the rail always remain planar and normal to the centroidal axis. Based on the assumption, we have the following results: (1) transverse normal stress components σ_{yy} and σ_{zz}, as shown in Figure 7, can be neglected compared to axial normal stress σ_{xx}; (2) the displacement fields at the centroidal axis of the rail cross-sections (u, v, and w) are functions of x only (Euler, 1744; Allen and Haisler, 1985; Grissom and Kerr, 2006).

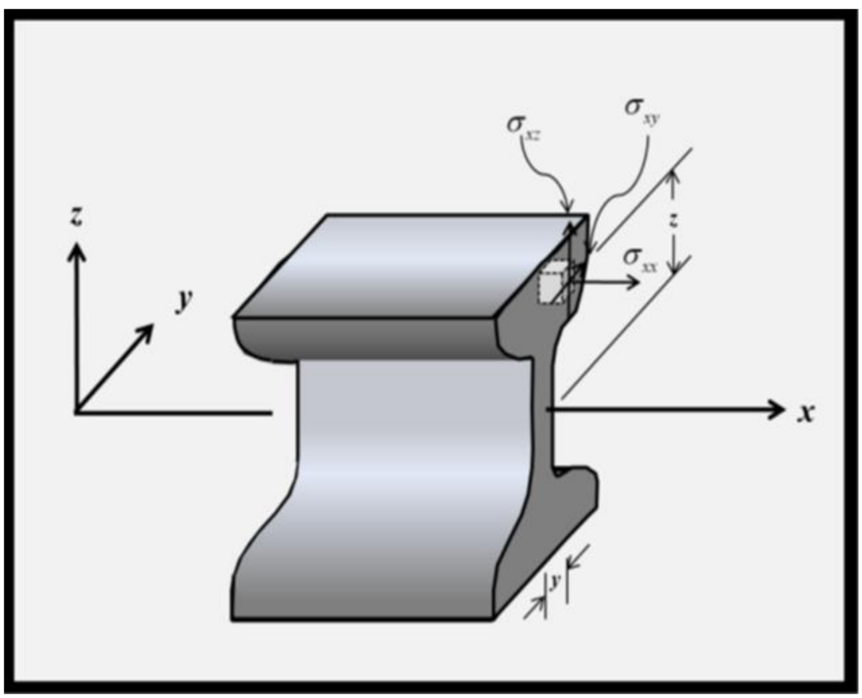

Figure 7 Demonstration of the normal stress components of an infinitesimal element within the rail (reprinted with permission from Allen and Fry, 2017)

According to field observations, rotation about the x-axis (torsion) is a relatively minor issue in rail buckling. Thus, a 3-D model with 5 degrees of freedom, excluding torsion, is developed herein. The x-y plane and x-z plane views of the free body diagram of the cut rail are shown in Figure 8 and Figure 9, respectively.

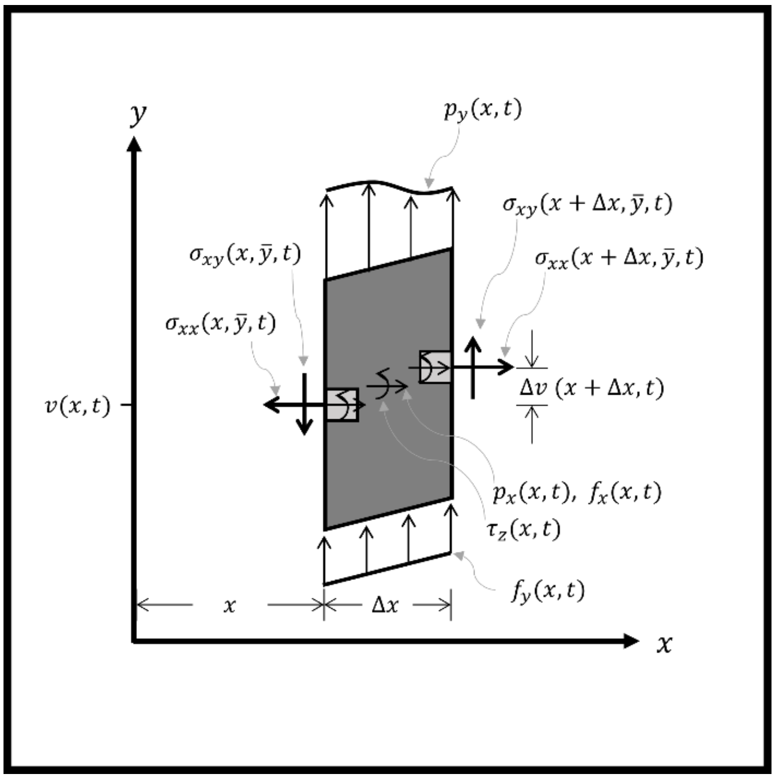

Figure 8 x-y plane view of the free body diagram of the cut rail

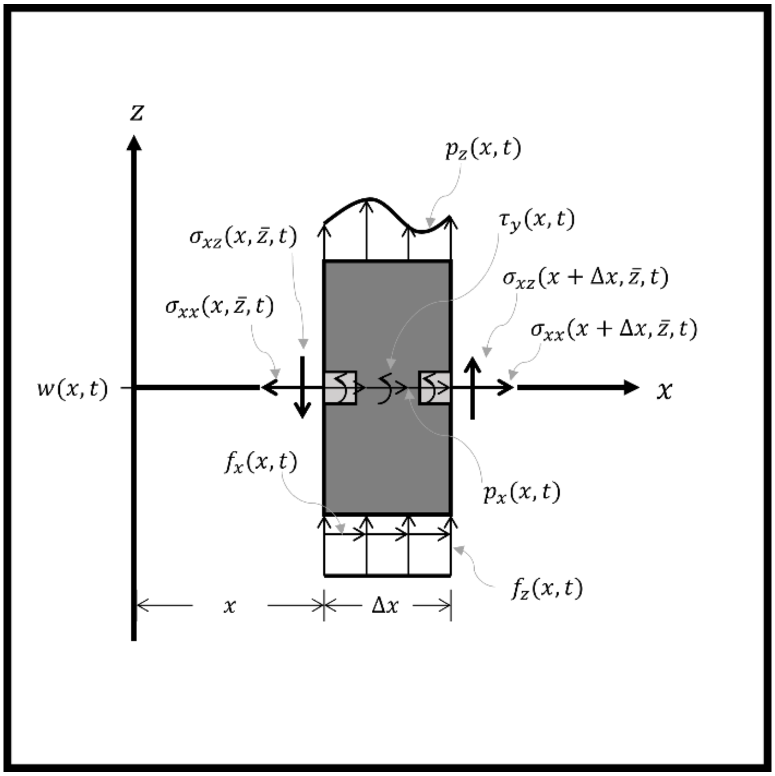

Figure 9 x-z plane view of the free body diagram of the cut rail

The symbols, σ_{xx}, σ_{yy}, σ_{zz}, σ_{xy}, and σ_{xz}, denote the stress components acting on the faces of the infinitesimal stress boxes located at the edges of the cut rail, while p_x, p_y, and p_z represent the external distributed loads acting in each respective direction. In addition, it can be noticed that stress components are not only functions of x and time (t), but also functions of $\bar{y}$, representing the lateral distance, and $\bar{z}$, representing the vertical distance, from the centroid. For simplification, the geometry of the rail cross-section is assumed to be symmetric about both the x-y and x-z planes. Additionally, all the loads and moments in this model are assumed to act through the centroid. Since the rail is considered homogeneous, the centroid and the neutral axis of the beam remain aligned throughout the deformation process. Finally, as shown in Figure 9,

τ_y represents the distributed moment caused by f_x, which acts at the bottom of the rail, and is given by:

$$\tau_y(x,t) = z^* \cdot f_x(x,t) \tag{11}$$

Where z^* is the moment arm, defined as the distance between the bottom of the rail and the centroid.

It should be noted that the x-y plane in Figure 8 is depicted as a deformed body, while the x-z plane in Figure 9 remains undeformed. The reason is that due to the difference between the moments of inertia I_{yy} and I_{zz}, buckling in the x-y plane happens much more frequently, and the geometric nonlinearity of this plane is also the main focus of this research. Even though vertical buckling can happen, but only when lateral displacements are constrained, it is rare. Thus, large vertical deformations are generally negligible and will not be considered in this research.

In accordance with Euler-Bernoulli beam theory, the force and moment resultants in the x-y and x-z planes are given as follows:

$$P(x,t) \equiv \int_A \sigma_{xx}\, dA \tag{12}$$

$$V_y(x,t) \equiv \int_A \sigma_{xy}\, dA \tag{13}$$

$$V_z(x,t) \equiv \int_A \sigma_{xz}\, dA \tag{14}$$

$$M_y(x,t) \equiv \int_A \sigma_{xx} \cdot \bar{z} dA \tag{15}$$

$$M_z(x,t) \equiv -\int_A \sigma_{xx} \cdot \bar{y} dA \tag{16}$$

Here, A is the cross-sectional area of the rail, P, V_y and V_z represent the axial, lateral and vertical resultant forces, respectively; and M_y and M_z are the resultant moments about the y-axis and z-axis, respectively. Additionally, using Equations (10) and (12) and assuming that A remains constant, the thermal load (P^T) of the track due to ΔT can then be defined as:

$$P^T = E \cdot A \cdot \alpha \cdot \Delta T \tag{17}$$

By utilizing Equations (12) to (16), the effects of stress components can be replaced by the resultant forces and moments as shown in Figure 10 and Figure 11.

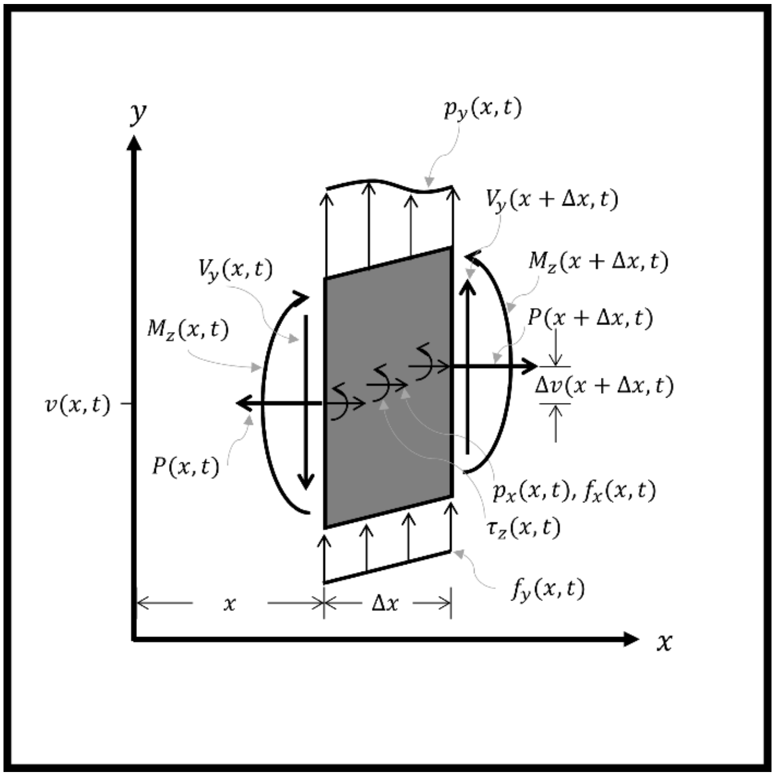

Figure 10 x-y plane view of the resultant forces and moment applied to a differential element of the rail

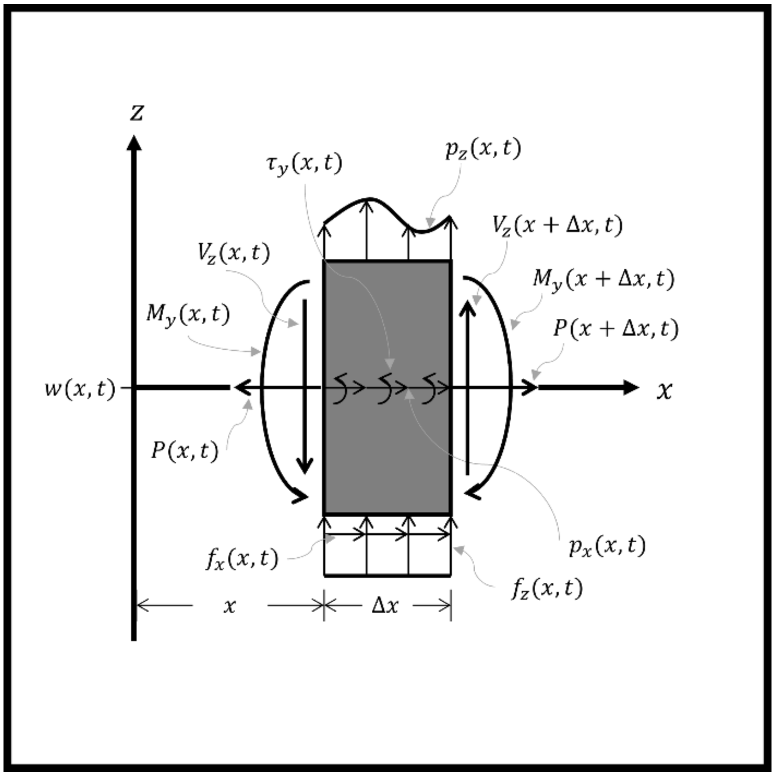

Figure 11 x-z plane view of the resultant forces and moment applied to a differential element of the rail

Given that the track length is extremely large compared to the deflection amplitude, it is reasonable to assume that the rotational angles are small and can be described by:

$$\theta_y \cong tan(\theta_y) = -\lim_{\Delta x \to 0} \frac{\Delta w}{\Delta x} = -\frac{dw}{dx} \tag{18}$$

$$\theta_z \cong tan(\theta_z) = \lim_{\Delta x \to 0} \frac{\Delta v}{\Delta x} = \frac{dv}{dx} \tag{19}$$

Regarding axial strain, the formulation when considering large deformations is expressed as:

$$\varepsilon_{xx} = \frac{du}{dx} + \frac{1}{2}\left[\left(\frac{du}{dx}\right)^2 + \left(\frac{dv}{dx}\right)^2 + \left(\frac{dw}{dx}\right)^2\right] \tag{20}$$

Since lateral displacements are significantly larger than the other two directions for the lateral bucking problem, the term $\frac{1}{2}\left(\frac{dv}{dx}\right)^2$ is the only second-order term that needs to be taken into consideration (Tvergaard and Needleman, 1981; Grissom and Kerr, 2006). Thus, the final strain-displacement relationship utilized herein is simplified as:

$$\varepsilon_{xx} = \frac{du}{dx} + \frac{1}{2}\left(\frac{dv}{dx}\right)^2 \tag{21}$$

Finally, since the problem is assumed to be quasi-static, t is no longer treated as an independent variable. As a result, when analyzing the displacement field (rather than the stress field), x remains the only independent variable for the problem. Applying all the detailed information above, we have constructed a well-posed initial quasi-static boundary value problem, as shown in Table 1:

Table 1: Initial boundary value problem for predicting rail response

1. **Independent variables:** x

2. **Known inputs:**

Loads: $p_x = p_x(x)$, $p_y = p_y(x)$, $p_z = p_z(x)$, $0 < x < L$

Temperature change: ΔT, known

Geometry: A, I_{yy}, I_{zz}, L, z^*

Material properties: E, α

Track parameters: k_x, $F_{y,lt}$, $F_{y,pk}$, v_{lt}, v_{pk}, λ_x, λ_y, d_{tie}, k_z, S

3. **Dependent variables:** $u = u(x)$, $v = v(x)$, $w = w(x)$, $P = P(x)$,

$V_y = V_y(x)$, $V_z = V_z(x)$, $M_y = M_y(x)$, $M_z = M_z(x)$

4. **Field equations:**

$$\frac{dP}{dx} = -p_x - f_x \tag{22}$$

$$\frac{dV_y}{dx} = -p_y - f_y \tag{23}$$

$$\frac{dV_z}{dx} = -p_z - f_z \tag{24}$$

$$\frac{dM_y}{dx} = V_z + z^* f_x \tag{25}$$

$$\frac{dM_z}{dx} = -V_y + P\frac{dv}{dx} - \tau_z \tag{26}$$

$$\frac{du}{dx} = \frac{P + P^T}{EA} - \frac{1}{2}\left(\frac{dv}{dx}\right)^2 \tag{27}$$

$$\frac{d^2v}{dx^2} = \frac{M_z}{EI_{zz}} \tag{28}$$

$$\frac{d^2w}{dx^2} = -\frac{M_y}{EI_{yy}} \tag{29}$$

5. **Auxiliary equations:** $f_x(u)$, $f_y(v)$, $f_z(w)$, $\tau_z(\theta_z)$, $P^T(\Delta T)$

There are 8 equations and 5 additional auxiliary equations (tie-ballast resistances, ballast vertical support, fastener rotational resistance, and the thermal load derived by the thermoelastic constitutive relation) for solving the listed 8 dependent variables. Even though the problem is well-posed, the highly coupled relations make it nonetheless rather difficult to obtain analytical solutions without making certain simplifying assumptions. As a result, in order to avoid deploying these necessarily debilitating assumptions, a numerical solving procedure utilizing FEM is proposed herein.

CHAPTER III

FINITE ELEMENT METHOD

To solve the eight coupled equations simultaneously without introducing excessive simplifications, the FEM is employed in this study. The process involves several key steps. First, the variational method is applied to derive the weak form of the original governing equations. Next, shape functions are introduced into the weak form to determine the system's stiffness matrix. Finally, depending on the requirements, either a force-control algorithm or a displacement-control algorithm is utilized. Additionally, iterative methods are incorporated into the algorithm to ensure convergence of the solutions. The detailed implementation of these steps is discussed in this chapter.

Variational Method

Since the governing differential equations are challenging to solve directly, the variational method reformulates them into integral forms, thereby weakening the solution in an averaged sense to effectively handle complex boundary conditions.

First, Equations (22), (23), and (24) represent Newton's Law of Motion along the three axes. By applying the Principle of Virtual Work, the three equations can be combined into the following single equation that needs to be solved:

$$\begin{aligned} &\int_0^L \left[\frac{dP}{dx} + p_x + f_x\right] \delta u \, dx \\ &+ \int_0^L \left[\frac{dV_y}{dx} + p_y + f_y\right] \delta v \, dx \\ &+ \int_0^L \left[\frac{dV_z}{dx} + p_z + f_z\right] \delta w \, dx = 0 \end{aligned} \tag{30}$$

Here, the δ symbol preceding the displacements indicates virtual displacements.

By integrating by parts for the $\frac{dP}{dx}$, $\frac{dV_y}{dx}$, and $\frac{dV_z}{dx}$ terms, the expression can be rewritten as:

$$-\int_0^L P\,\delta\frac{du}{dx}\,dx + [P\delta u]_0^L + \int_0^L p_x\,\delta u\,dx + \int_0^L f_x\,\delta u\,dx$$

$$-\int_0^L V_y\,\delta\frac{dv}{dx}\,dx + \left[V_y\delta v\right]_0^L + \int_0^L p_y\,\delta v\,dx + \int_0^L f_y\,\delta v\,dx \tag{31}$$

$$-\int_0^L V_z\,\delta\frac{dw}{dx}\,dx + [V_z\delta w]_0^L + \int_0^L p_z\,\delta w\,dx + \int_0^L f_z\,\delta w\,dx = 0$$

Next, by substituting Equations (25), (26), and (27) into the expression above, and through further rearrangements, we arrive at:

$$
\begin{aligned}
&-\int_0^L \left[EA\frac{du}{dx} + \frac{EA}{2}\left(\frac{dv}{dx}\right)^2 - P^T\right] \delta\frac{du}{dx}\ dx \\
&+\int_0^L \frac{dM_z}{dx}\delta\frac{dv}{dx}\ dx - \int_0^L \left[EA\frac{du}{dx} + \frac{EA}{2}\left(\frac{dv}{dx}\right)^2 - P^T\right] \frac{dv}{dx}\delta\frac{dv}{dx}\ dx \\
&-\int_0^L \frac{dM_y}{dx}\delta\frac{dw}{dx}\ dx \\
&+\int_0^L f_x\ \delta u\ \ dx + \int_0^L f_y\ \delta v\ \ dx + \int_0^L f_z\ \delta w\ \ dx \\
&+\int_0^L z^* f_x\ \delta\frac{dw}{dx}\ dx + \int_0^L \tau_z\ \delta\frac{dv}{dx}\ dx \\
&+\int_0^L p_x\ \delta u\ \ dx + \int_0^L p_y\ \delta v\ \ dx + \int_0^L p_z\ \delta w\ \ dx \\
&+[P\ \delta u]_0^L + \left[V_y\ \delta v\right]_0^L + [V_z\ \delta w]_0^L = 0
\end{aligned} \tag{32}
$$

By applying integration by parts once more to terms involving $\frac{dM_y}{dx}$ and $\frac{dM_z}{dx}$, and rearranging further, obtain:

$$
\begin{gathered}
-\int_0^L EA\frac{du}{dx}\,\delta\frac{du}{dx}\,dx-\int_0^L M_z\,\delta\frac{d^2v}{dx^2}\,dx+\int_0^L M_y\,\delta\frac{d^2w}{dx^2}\,dx \\
-\int_0^L \frac{EA}{2}\left(\frac{dv}{dx}\right)^2\,\delta\frac{du}{dx}\,dx \\
-\int_0^L EA\frac{du}{dx}\frac{dv}{dx}\delta\frac{dv}{dx}\,dx-\int_0^L \frac{EA}{2}\left(\frac{dv}{dx}\right)^3\,\delta\frac{dv}{dx}\,dx \\
+\int_0^L P^T\,\delta\frac{du}{dx}\,dx+\int_0^L P^T\frac{dv}{dx}\delta\frac{dv}{dx}\,dx \\
+\int_0^L f_x\,\delta u\,dx+\int_0^L f_y\,\delta v\,dx+\int_0^L f_z\,\delta w\,dx \\
+\int_0^L z^* f_x\,\delta\frac{dw}{dx}\,dx+\int_0^L \tau_z\,\delta\frac{dv}{dx}\,dx \\
+\int_0^L p_x\,\delta u\,dx+\int_0^L p_y\,\delta v\,dx+\int_0^L p_z\,\delta w\,dx \\
+[P\,\delta u]_0^L+\left[V_y\,\delta v\right]_0^L+[V_z\,\delta w]_0^L-\left[M_y\,\delta\frac{dw}{dx}\right]_0^L+\left[M_z\,\delta\frac{dv}{dx}\right]_0^L=0
\end{gathered}
\tag{33}
$$

Finally, applying Equations (18), (19), (28), and (29), we derive the final weak form that needs to be solved for the boundary value problem.

$$
\begin{aligned}
&-\int_0^L EA\frac{du}{dx}\delta\frac{du}{dx}\ dx-\int_0^L EI_{zz}\frac{d^2v}{dx^2}\delta\frac{d^2v}{dx^2}\ dx-\int_0^L EI_{yy}\frac{d^2w}{dx^2}\delta\frac{d^2w}{dx^2}\ dx\\
&-\int_0^L \frac{EA}{2}\left(\frac{dv}{dx}\right)^2\delta\frac{du}{dx}\ dx\\
&-\int_0^L EA\frac{du}{dx}\frac{dv}{dx}\delta\frac{dv}{dx}\ dx-\int_0^L \frac{EA}{2}\left(\frac{dv}{dx}\right)^3\delta\frac{dv}{dx}\ dx\\
&+\int_0^L P^T\ \delta\frac{du}{dx}\ dx+\int_0^L P^T\frac{dv}{dx}\delta\frac{dv}{dx}\ dx\\
&+\int_0^L f_x\ \delta u\ \ dx+\int_0^L f_y\ \delta v\ \ dx+\int_0^L f_z\ \delta w\ \ dx\\
&+\int_0^L z^* f_x\ \delta\frac{dw}{dx}\ dx+\int_0^L \tau_z\ \delta\frac{dv}{dx}\ dx\\
&+\int_0^L p_x\ \delta u\ \ dx+\int_0^L p_y\ \delta v\ \ dx+\int_0^L p_z\ \delta w\ \ dx\\
&+[P\ \delta u]_0^L+\left[V_y\ \delta v\right]_0^L+[V_z\ \delta w]_0^L+\left[M_y\ \delta\theta_y\right]_0^L+[M_z\ \delta\theta_z]_0^L=0
\end{aligned}
\tag{34}
$$

As we can see, there are several different sources of nonlinearity such as: geometric nonlinearity (term 5 and term 6), nonlinearity caused by strain-displacement relationship (term 4, term 6), and nonlinearity caused by lateral tie-ballast resistance (term 10). In addition, though not shown in the weak formulation, nonlinearities caused by point loads and moments will also be included in this model, entering the system by specifying realistic boundary conditions.

Shape Functions

To solve the weak form with the finite element method, the global domain is first discretized into local elements, allowing the model to capture local displacement changes effectively, as shown in Figure 12.

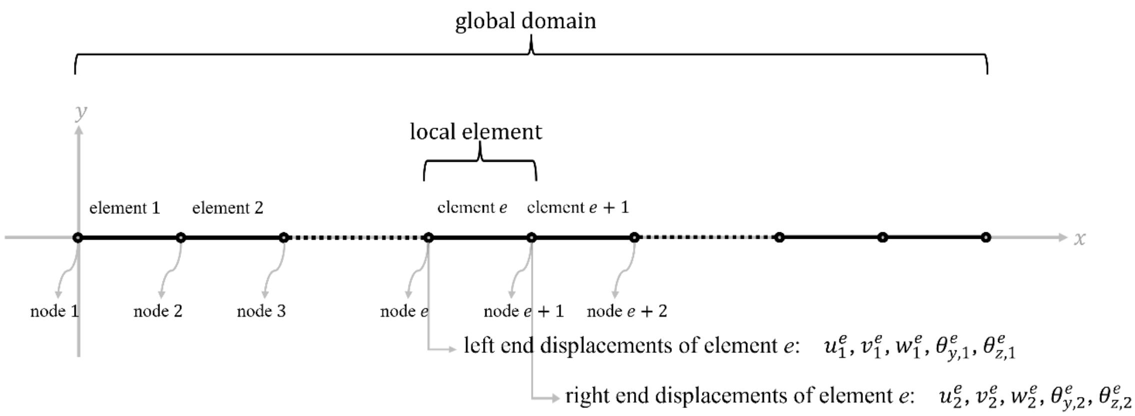

Figure 12 Schematic of the mesh showing local element displacements at the nodes

To ensure smooth and accurate representations of bending deformations, Hermitian shape functions of cubic order (Allen and Haisler, 1985) are employed in this research. These functions can be used to describe displacements, expressed as:

$$u^e = \sum_{n=1}^{10} \xi_n q_n^e \tag{35}$$

$$v^e = \sum_{n=1}^{10} \eta_n q_n^e \tag{36}$$

$$w^e = \sum_{n=1}^{10} \zeta_n q_n^e \tag{37}$$

The superscript e on the displacements indicates local element displacements, represents the components of the local element displacement vector ($\boldsymbol{q}^e$), which has a size of 10. The vector is expressed as:

$$\boldsymbol{q}^e = [u_1^e \quad v_1^e \quad w_1^e \quad \theta_{y,1}^e \quad \theta_{z,1}^e \quad u_2^e \quad v_2^e \quad w_2^e \quad \theta_{y,2}^e \quad \theta_{z,2}^e]^T \tag{38}$$

Here, the subscripts 1 and 2 refer to the left end and right end of the local element, respectively. The Hermitian shape functions ξ_n, η_n, and ζ_n are defined as follows:

$$\xi_n = \begin{cases} 1 - \dfrac{x}{L^e}, & n = 1 \\ \dfrac{x}{L^e}, & n = 6 \\ 0, & else \end{cases} \quad , for\ 0 < x < L^e \tag{39}$$

$$\eta_n = \begin{cases} 1 - 3\left(\dfrac{x}{L^e}\right)^2 + 2\left(\dfrac{x}{L^e}\right)^3, & n = 2 \\ x\left(1 - \dfrac{x}{L^e}\right)^2, & n = 5 \\ 3\left(\dfrac{x}{L^e}\right)^2 - 2\left(\dfrac{x}{L^e}\right)^3, & n = 7 \\ x\left[\left(\dfrac{x}{L^e}\right)^2 - \dfrac{x}{L^e}\right], & n = 10 \\ 0, & else \end{cases} \quad , for\ 0 < x < L^e \tag{40}$$

$$\zeta_n = \begin{cases} 1 - 3\left(\frac{x}{L^e}\right)^2 + 2\left(\frac{x}{L^e}\right)^3, & n = 3 \\ -x\left(1 - \frac{x}{L^e}\right)^2, & n = 4 \\ 3\left(\frac{x}{L^e}\right)^2 - 2\left(\frac{x}{L^e}\right)^3, & n = 8 \\ -x\left[\left(\frac{x}{L^e}\right)^2 - \frac{x}{L^e}\right], & n = 9 \\ 0, & else \end{cases} \quad , for\ 0 < x < L^e \tag{41}$$

Where L^e denotes the length of the local element.

Stiffness Matrix Derivation

To solve the weak formulation, the shape functions are substituted into Equation (34), leading to the following relation:

$$\sum_{i=1}^{10} (I_i^e - F_i^e)\ \delta q_i^e = 0 \tag{42}$$

where:

$$I_i^e = I_{Lin,i}^e + I_{LS,i}^e + I_{Geo,i}^e + I_{LS,Geo,i}^e + I_{T,i}^e + I_{Lon,i}^e + I_{Lat,i}^e + I_{Bal,i}^e + I_{Fas,i}^e \tag{43}$$

$$F_i^e = \int_0^{L^e} \left[p_x \xi_i + p_y \eta_i + p_z \zeta_i + P^T \frac{d\xi_i}{dx} \right] dx \tag{44}$$

Here, I_i^e is a functional that depends on functions defined by q_i^e, and F_i^e represents the force vector capturing the effects of applied external loads (or temperature change). Each sub-term of I_i^e is defined below:

$$\begin{aligned} I_{Lin,i}^e = \int_0^{L^e} [\, EA \frac{d}{dx} \left(\sum_{m=1}^{10} \xi_m\, q_m^e \right) \frac{d\xi_i}{dx} + EI_{zz} \frac{d^2}{dx^2} \left(\sum_{m=1}^{10} \eta_m\, q_m^e \right) \frac{d^2 \eta_i}{dx^2} \\ + EI_{yy} \frac{d^2}{dx^2} \left(\sum_{m=1}^{10} \zeta_m\, q_m^e \right) \frac{d^2 \zeta_i}{dx^2}] dx \end{aligned} \tag{45}$$

$$I_{LS,i}^e = \int_0^{L^e} \left[\frac{EA}{2} \frac{d}{dx} \left(\sum_{m=1}^{10} \eta_m\, q_m^e \right) \frac{d}{dx} \left(\sum_{n=1}^{10} \eta_n\, q_n^e \right) \frac{d\xi_i}{dx} \right] dx \tag{46}$$

$$I_{Geo,i}^{e} = \int_{0}^{L^e} \left[EA \frac{d}{dx} \left(\sum_{m=1}^{10} \xi_m \, q_m^e \right) \frac{d}{dx} \left(\sum_{n=1}^{10} \eta_n \, q_n^e \right) \frac{d\eta_i}{dx} \right] dx \tag{47}$$

$$I_{LS,Geo,i}^{e} = \int_{0}^{L^e} \left[\frac{EA}{2} \frac{d}{dx} \left(\sum_{m=1}^{10} \eta_m \, q_m^e \right) \frac{d}{dx} \left(\sum_{n=1}^{10} \eta_n \, q_n^e \right) \frac{d}{dx} \left(\sum_{r=1}^{10} \eta_r \, q_r^e \right) \frac{d\eta_i}{dx} \right] dx \tag{48}$$

$$I_{T,i}^{e} = -\int_{0}^{L^e} \left[P^T \frac{d}{dx} \left(\sum_{m=1}^{10} \eta_m \, q_m^e \right) \frac{d\eta_i}{dx} \right] dx \tag{49}$$

$$I_{Lon,i}^{e} = -\int_{0}^{L^e} f_x \, \xi_i \; dx - \int_{0}^{L^e} z^* f_x \frac{d\zeta_i}{dx} \, dx \tag{50}$$

$$I_{Lat,i}^{e} = -\int_{0}^{L^e} f_y \, \eta_i \; dx \tag{51}$$

$$I_{Bal,i}^{e} = -\int_{0}^{L^e} f_z \, \zeta_i \; dx \tag{52}$$

$$I_{Fas,i}^{e} = -\int_{0}^{L^e} \tau_z \, \frac{d\eta_i}{dx} \, dx \tag{53}$$

Here, $I_{Lin,i}^{e}$ represents the terms caused by axial stiffness and bending stiffness, which are linear. The terms $I_{LS,i}^{e}$ account for large strain effects in the axial direction. While $I_{Geo,i}^{e}$ capture the effects of geometric nonlinearity, $I_{LS,Geo,i}^{e}$ represents the combined contributions of geometric nonlinearity when considering large strain effects. The terms $I_{T,i}^{e}$, $I_{Lon,i}^{e}$, $I_{Lat,i}^{e}$, $I_{Bal,i}^{e}$, $I_{Fas,i}^{e}$

correspond to effects of secondary moments caused by thermal loads, longitudinal tie-ballast resistance, lateral tie-ballast resistance, vertical ballast resistance, and fastener rotational resistance, respectively.

It is also important to note that the resultant force and moment terms at the boundaries have been omitted because they will cancel out each other when assembling from local form into global form.

Since δq_i^e should be mutually linear independent, and Equation (42) must hold for all cases, this leads to a system of 10 equations:

$$I_i^e = F_i^e, \text{ for } i = 1 \text{ to } 10 \tag{54}$$

To solve this system, a Taylor expansion is applied. If we expand against $I_i^e\left(q_j^e\right)$:

$$I_i^e\left(q_j^e + \Delta q_j^e\right) = I_i^e\left(q_j^e\right) + \frac{\partial I_i^e}{\partial q_j^e}\Delta q_j^e + \frac{1}{2}\frac{\partial^2 I_i^e}{\partial {q_j^e}^2}\left(\Delta q_j^e\right)^2 + H.O.T \tag{55}$$

As the displacement increments between different time-steps are relatively small, we can neglect higher-order terms ($H.O.T$). Only considering zero and first-order terms, we obtain the following:

$$K_{ij}^e \Delta q_j^e = I_i^e\left(q_j^e + \Delta q_j^e\right) - I_i^e\left(q_j^e\right) \tag{56}$$

The Jacobian matrix of I_i^e, or so-called the stiffness matrix, is defined by:

$$K_{ij}^e = \frac{\partial I_i^e}{\partial q_j^e} \tag{57}$$

By combining Equations (43) and (57), K_{ij}^e could also be split into sub-terms:

$$K_{ij}^e = K_{Lin,ij}^e + K_{LS,ij}^e + K_{Geo,ij}^e + K_{LS,Geo,ij}^e + K_{T,ij}^e + K_{Lon,ij}^e + K_{Lat,ij}^e + K_{Bal,ij}^e + K_{Fas,ij}^e \quad (58)$$

Each sub-term of K_i^e is defined below:

$$K_{Lin,ij}^e = \int_0^{L^e} [\, EA \frac{d\xi_i}{dx}\frac{d\xi_j}{dx} + EI_{zz}\frac{d^2\eta_i}{dx^2}\frac{d^2\eta_j}{dx^2} + EI_{yy}\frac{d^2\zeta_i}{dx^2}\frac{d^2\zeta_j}{dx^2}]dx \quad (59)$$

$$K_{LS,ij}^e = \int_0^{L^e} \left[EA\frac{d}{dx}\left(\sum_{m=1}^{10}\eta_m\, q_m^e\right)\frac{d\xi_i}{dx}\frac{d\eta_j}{dx}\right]dx \quad (60)$$

$$K_{Geo,ij}^e = \int_0^{L^e} \left[EA\frac{d}{dx}\left(\sum_{m=1}^{10}\eta_m\, q_m^e\right)\frac{d\eta_i}{dx}\frac{d\xi_j}{dx}\right]dx + \int_0^{L^e} \left[EA\frac{d}{dx}\left(\sum_{m=1}^{10}\xi_m\, q_m^e\right)\frac{d\eta_i}{dx}\frac{d\eta_j}{dx}\right]dx \quad (61)$$

$$K_{LS,Geo,ij}^e = \int_0^{L^e} \left[\frac{3EA}{2}\frac{d}{dx}\left(\sum_{m=1}^{10}\eta_m\, q_m^e\right)\frac{d}{dx}\left(\sum_{n=1}^{10}\eta_n\, q_n^e\right)\frac{d\eta_i}{dx}\frac{d\eta_j}{dx}\right]dx \quad (62)$$

$$K_{T,ij}^e = -\int_0^{L^e} \left[P^T\frac{d\eta_i}{dx}\frac{d\eta_j}{dx}\right]dx \quad (63)$$

$$K_{Lon,ij}^e = -\int_0^{L^e} \xi_i\frac{\partial f_x}{\partial q_j^e}\, dx - \int_0^{L^e} z^*\frac{d\zeta_i}{dx}\frac{\partial f_x}{\partial q_j^e}\, dx \quad (64)$$

$$K_{Lat,ij}^{e} = -\int_{0}^{L^e} \eta_i \frac{\partial f_y}{\partial q_j^e}\, dx \tag{65}$$

$$K_{Bal,ij}^{e} = -\int_{0}^{L^e} \zeta_i \frac{\partial f_z}{\partial q_j^e}\, dx \tag{66}$$

$$K_{Fas,ij}^{e} = -\int_{0}^{L^e} \frac{d\eta_i}{dx} \frac{\partial \tau_z}{\partial q_j^e}\, dx \tag{67}$$

It should be clear that f_x, f_z, and τ_z are all linear functions of the corresponding displacements as shown in Equations (3), (4), (5), (7), (8), and (9). Thus, the partial derivatives in $K_{Lon,i}^{e}$, $K_{Bal,i}^{e}$, and $K_{Fas,i}^{e}$ could be calculated directly, as shown:

$$K_{Lon,ij}^{e} = \frac{\lambda_x \cdot k_x}{d_{tie}} \cdot \left[\int_{0}^{L^e} \xi_i\ \xi_j\ dx + \int_{0}^{L^e} z^* \frac{d\zeta_i}{dx}\ \xi_j\ dx\right] \tag{68}$$

$$K_{Bal,ij}^{e} = \frac{k_z}{d_{tie}} \int_{0}^{L^e} \zeta_i \zeta_j\ dx \tag{69}$$

$$K_{Fas,ij}^{e} = \frac{S}{d_{tie}} \int_{0}^{L^e} \frac{d\eta_i}{dx} \frac{d\eta_j}{dx}\, dx \tag{70}$$

For $K_{Lat,i}^{e}$, the integrand contains the partial derivative of f_y, which is either a bilinear or trilinear function based on the given ballast condition. Due to this, additional treatment is required before $K_{Lat,i}^{e}$ can be calculated. First, the partial derivative is determined as follows:

- Disturbed condition (bilinear formulation):

$$\frac{\partial f_y}{\partial q_j^e} = \begin{cases} -\dfrac{\lambda_y}{d_{tie}} \dfrac{F_{y,lt}}{v_{lt}} \eta_j, & |v^e| \leq v_{lt} \\ 0, & |v^e| > v_{lt} \end{cases} \tag{71}$$

- Compacted condition (trilinear formulation):

$$\frac{\partial f_y}{\partial q_j^e} = \begin{cases} -\dfrac{\lambda_y}{d_{tie}} \dfrac{F_{y,pk}}{v_{pk}} \eta_j, & |v^e| \leq v_{pk} \\ -\dfrac{\lambda_y}{d_{tie}} \dfrac{F_{y,lt} - F_{y,pk}}{v_{lt} - v_{pk}} \eta_j, & v_{pk} < |v^e| \leq v_{lt} \\ 0, & |v^e| > v_{lt} \end{cases} \tag{72}$$

Based on this formulation, it is evident that $K_{Lat,i}^e$ can be calculated if split into several integrals. Since the disturbed condition is a simplified version of the compacted condition, the compacted condition is used as an example:

$$K_{Lat,ij}^e = \frac{\lambda_y \cdot k_{y,1}}{d_{tie}} \int_0^{L_1^e} \eta_i \eta_j \, dx + \frac{\lambda_y \cdot k_{y,2}}{d_{tie}} \int_0^{L_2^e} \eta_i \eta_j \, dx \tag{73}$$

Here, $k_{y,1}$ and $k_{y,2}$ represent the slopes of the STPT curve-fitting result for different sections:

$$k_{y,1} = \frac{F_{y,pk}}{v_{pk}} \tag{74}$$

$$k_{y,2} = \frac{F_{y,lt} - F_{y,pk}}{v_{lt} - v_{pk}} \tag{75}$$

The lengths L_1^e and L_2^e correspond to the effective sections of the element satisfying the conditions $|v^e| \leq v_{pk}$ and $v_{pk} < |v^e| \leq v_{lt}$, respectively. For this case, v^e is assumed to vary linearly along the element, and can be written as:

$$v^e(x) = v_1^e + \frac{v_2^e - v_1^e}{L^e}x, \qquad 0 \leq x \leq L^e \tag{76}$$

A more detailed illustration is shown in Figure 13:

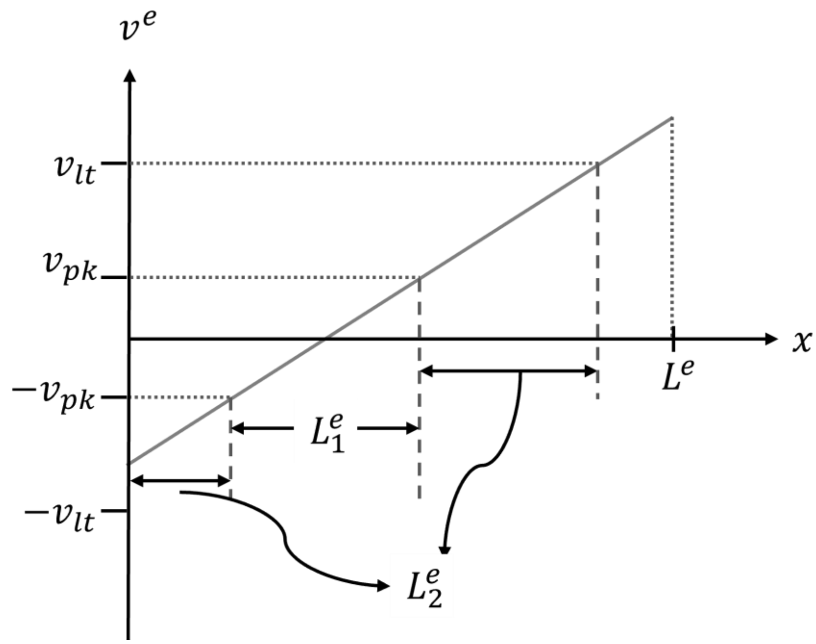

Figure 13 Linear distribution of lateral displacements along the element, showing effective lengths for the compacted ballast condition

Using the procedure described above, $K_{Lat,i}^e$ effectively captures the lateral tie-ballast resistance and addresses its nonlinearity. This process must be applied individually to each element.

All sub-terms of K_i^e are now well-defined. Instead of using numerical integration methods such as quadrature, these terms can be computed a priori to reduce simulation time. Detailed calculation results for K_i^e and F_i^e are provided in Appendix A.

Regarding Equation (54), we obtain the following final form of the incremental equilibrium equations:

$$K_{ij}^{e} \varDelta q_{j}^{e} = \varDelta F_{i}^{e} \tag{77}$$

$$\varDelta F_{i}^{e} = F_{i}^{e}\left(q_{j}^{e} + \varDelta q_{j}^{e}\right) - F_{i}^{e}\left(q_{j}^{e}\right) \tag{78}$$

Utilizing the standard FE assembly method, the local stiffness matrices and force vectors are assembled into the global form, K_{ij} and ΔF_{i}, to model the entire rail section:

$$K_{ij} \varDelta q_{j} = \varDelta F_{i} \tag{79}$$

It is important to note that K_{ij} is a function of the global displacement vector, expressed as $K_{ij} = K_{ij}(q_{j})$, thereby incorporating the nonlinearities into the formulation.

Force-Control Algorithm

The force-control algorithm is used to model rail buckling under either mechanical or thermal loads. In order to accurately account for the nonlinearities within K_{ij}, the entire loading procedure is divided into multiple time-steps. At each time-step, an equal increment of load or temperature change is applied, and each step is assumed to remain quasi-static. The displacement values used to compute K_{ij} must be updated at every time-step, and for greater accuracy, iterative methods, such as Newton's method are deployed within this model. The iterative version of Equation (79) for force control can be expressed as:

$$R_i^m = R_i\left(\Delta q_j^m\right) = K_{ij}^m \Delta q_j^m - \Delta F_i^m \tag{80}$$

where:

$$K_{ij}^m = K_{ij}\left(q_j^m\right) \tag{81}$$

$$q_j^m = q_{j,old} + \Delta q_j^m \tag{82}$$

Here, the superscript m denotes the iteration number within the time-step, and $q_{j,old}$ refers to the global displacement vector from the previous time-step. The term R_i^m is the load residual, quantifying the imbalance between the applied load (ΔF_i^m) and reaction load corresponding to the current displacement change ($K_{ij}^m \Delta q_j^m$). The goal of the iterative process is to minimize R^m and ensure that the system reaches equilibrium.

Before initiating the iterative process, the initial guess for Equation (131) (with $m = 1$) must be provided. It can be obtained by:

$$\Delta q_j^1 = \left(K_{ij}^{old}\right)^{-1} \Delta F_i \tag{83}$$

Here, $\left(K_{ij}^{old}\right)^{-1}$ is the inverse of K_{ij}^{old}=$K_{ij}(q_{j,old})$. Once Δq_j^1 is obtained, the iterative process can proceed.

The concept of Newton's method is to use results from previous iterations to obtain an improved estimate for the next iteration. The procedure is terminated when it satisfies a convergence criterion related to the Euclidean norm of the residual, $\left||R_i^m|\right|$, which must fall below a pre-determined threshold, close to 0.

Using Taylor's Formula to expand R_i^m against Δq_j^m while neglecting higher order terms results in:

$$R_i^m = -\frac{\partial R_i^m}{\partial \Delta q_j}\left(\Delta q_j^{m+1} - \Delta q_j^m\right) \tag{84}$$

Here, $\frac{\partial R_i^m}{\partial \Delta q_j^m}$ is the Jacobian of the residual, which indicates the load residual change rate at iteration m.

Equation (84) is then used to obtain the displacement change vector at iteration $m+1$, Δq_j^{m+1}. Equations (131) and (84) are solved repeatedly until $\left||R_i^m|\right|$ satisfied the convergence criterion, which is set to 6×10^{-6} in this research.

Once this condition is satisfied, it indicates that the difference between Δq_j^m and Δq_j^{m+1} is negligible, so convergence at the time-step is reached. The updated global displacement vector $q_{j,new}$, which will be used in the next step, can be obtained by combining the displacement vector from the previous step, $q_{j,old}$, and the converged displacement change vector, Δq_j^m:

$$q_{j,new} = q_{j,old} + \Delta q_j^m \tag{85}$$

In practice, calculating $\frac{\partial R_i^m}{\partial \Delta q_j}$ is time-consuming and non-efficient. Thus, the Krylov subspace method is applied (Knoll and Keyes, 2004), where it utilizes the Generalized Minimal RESidual method (GMRES) (Saad and Schultz, 1986) approximate the Jacobian matrix with sub-iterations. The Newton-Krylov method has proven to be a highly efficient nonlinear system-solving procedure and has already been included in the current SciPy Module (Virtanen et al., 2020), this research utilizes this well-known function to solve the problem demonstrated.

As axial load is applied to the rail, The corresponding load vs. displacement curve can be found by tracking the displacements at each load step, as shown in Figure 14.

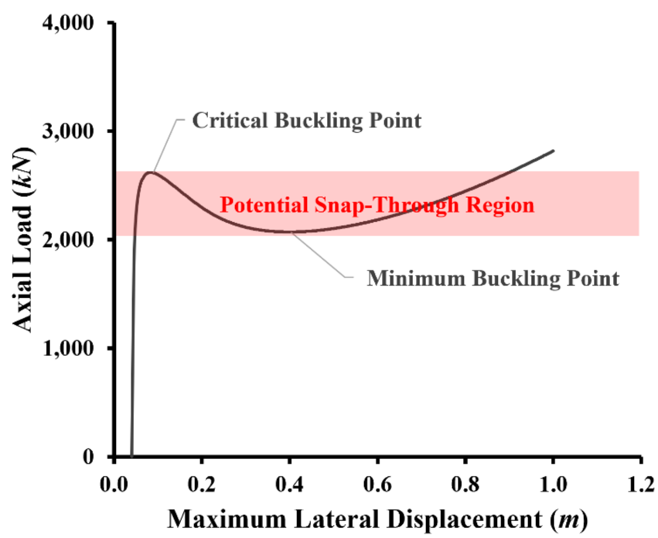

Figure 14 Demonstration of the axial load vs. maximum lateral displacement curve for a rail buckling problem while using force control

As the applied load value increases, the slope of the curve abruptly decreases, a phenomenon referred to as softening. For most cases, the displacement path can experience snap-through at the first unstable point as the load has reached its local maximum. In other cases, the curve could stiffen again, a process called progressive buckling and does not have a significant unstable trend. Some researchers have shown that the value of the lateral tie-ballast resistance could cause the difference between these two cases (Samavedam et al., 1993; Kish and Samavedam, 2013). In this research, we define the displacement where the slope of the load vs. displacement curve becomes 0 as the critical buckling displacement (v_{cr}) and the corresponding load as the critical buckling load (P_{cr}).

Displacement-Control Algorithm

While the force-control algorithm is sufficient for determining P_{cr}, the rail may buckle under lower axial loads if additional energy is introduced to the system, such as from loads caused by vehicle movement (Kish and Samavedam, 2013). Since the force-control algorithm does not permit negative load changes, it is incapable of capturing the equilibrium load vs. displacement path when softening occurs beyond the critical buckling point. Therefore, the displacement-control algorithm is utilized in this research.

The displacement-control algorithm incrementally increases the lateral displacement at a specified point and calculates the corresponding axial load required to produce this change. In this study, the buckling geometry is assumed to be symmetric about the midpoint, making the midpoint—where the maximum lateral displacement occurs—the control point. The algorithm is adapted from the self-correcting method for displacement incrementation introduced by Haisler, Stricklin, and Key (1977), with modifications implemented to address the specific needs of rail buckling analysis.

As with the force-control algorithm, the displacement-control process involves time-stepping and iterative methods. The process begins with Equation (80), (81), and (82). However, since the applied force increment (ΔF_i^1) is an unknown, the initial displacement change vector, Δq_j^1, cannot be determined using Equation (83). Instead, an alternative approach is applied:

$$K_{ij}^{old} \Delta q_j^1 = \Delta F_i^1 \tag{86}$$

By partitioning K_{ij}^{old}, Δq_j^1, and ΔF_i^1 into sub-matrices and vectors, Equation (86) is rewritten as:

$$K_{ff,ij}^{old}\Delta q_{f,j}^{1} + K_{fc,ij}^{old}\Delta q_{c,j}^{1} = \Delta F_{f,i}^{1} = \Delta P^{1} f_{f,i} \quad (87)$$

$$K_{cf,ij}^{old}\Delta q_{f,j}^{1} + K_{cc,ij}^{old}\Delta q_{c,j}^{1} = \Delta F_{c,i}^{1} = \Delta P^{1} f_{c,i} \quad (88)$$

Here, Subscripts f and c represent "free" and "constrained" degrees of freedom, respectively. The vector Δq_f^1 contains nodal displacement change values that are free to vary during the simulation. While Δq_c^1 contains constrained nodal displacement changes, which are prescribed by displacement boundary conditions and the displacement control point, these values are known. ΔP^1 is a scalar representing the magnitude of the applied load, while $f_{f,i}$ and $f_{c,i}$ are vectors of 0s and 1s, indicating where load changes are applied. Since an external axial load is assumed to act only at the left end to induce rail buckling, $f_{c,i}$ simplifies to a zero vector, and $f_{f,i}$ contains a single non-zero element with a value of 1, corresponding to the axial load at the left end.

Rewriting Equation (87), $\Delta q_{f,j}^1$ is expressed as:

$$\Delta q_{f,j}^{1} = A_j + \Delta P^{1} B_j \quad (89)$$

where A_j and B_j are defined as:

$$K_{ff,ij}^{old} A_j = -K_{fc,ij}^{old}\Delta q_{c,j}^{1} \quad (90)$$

$$K_{ff,ij}^{old} B_j = f_{f,i} \quad (91)$$

By solving A_j and B_j and substituting into Equation (89), $\Delta q^1_{f,j}$ expressed by ΔP^1 is obtained. Substituting this result into Equation (88) yields:

$$\Delta P^1\left(K^{old}_{cf,ij}B_j - f_{c,i}\right) = -K^{old}_{cf,ij}A_j - K^{old}_{cc,ij}\Delta q^1_{c,j} \tag{92}$$

Since both sides of Equation (92) are vectors of the same size, element-wise division is used to calculate ΔP^1.

Using the predefined $\Delta q^1_{c,j}$, $f_{c,i}$, and $f_{f,i}$, along with $\Delta q^1_{c,j}$ and ΔP^1 obtained above, the global displacement change vector Δq^1_j and global load change vector ΔF^1_i at the first iteration can be determined. With K^1_{ij} updated using Δq^1_j, the force residual, R^1_i is then calculated via Equation (80), completing the calculation for the first iteration (m=1).

If $\left|\left|R^1_i\right|\right|$ does not satisfy the convergence criterion specified in the force-control algorithm, the iteration process continues. For iteration $m > 1$, Δq^m_j and ΔF^m_i are determined using:

$$K^{m-1}_{ij}\Delta q^m_j = \Delta F^m_i \tag{93}$$

Introducing the displacement correction vector ($\Delta\Delta q^m_j$) and force correction vector ($\Delta\Delta F^m_i$):

$$\Delta\Delta q^m_j = \Delta q^m_j - \Delta q^{m-1}_j \tag{94}$$

$$\Delta\Delta F^m_i = \Delta F^m_i - \Delta F^{m-1}_i \tag{95}$$

Equation (93) can be rewritten as:

$$K_{ij}^{m-1}\Delta\Delta q_j^m = \Delta\Delta F_i^m - R_i^{m-1} \tag{96}$$

The equation above can be solved by similar procedures outlined in Equations (87) to (92). This process is repeated until the convergence criterion is satisfied.

By utilizing the displacement-control algorithm, the simulation can continue even when softening occurs in rail buckling. Beyond the softening point, the load vs. displacement curve stiffens again, likely due to the nonlinear term $\frac{1}{2}\left(\frac{dv}{dx}\right)^2$ in the axial strain-displacement relationship. The point where the slope of the curve changes direction is referred to as the minimum buckling point, characterized by the minimum buckling load (P_{min}) and the minimum buckling lateral displacement (v_{min}). It is termed the minimum buckling point because axial loads lower than P_{min} cannot induce buckling, even with external energy input, as no corresponding equilibrium state exists.

Model Verification

The algorithm presented herein has been implemented in the Python code "AAR/TAMU Track Buckle Model", and previously verified against several analytical solutions (Musu, 2021). However, with modifications to the model, additional test cases are introduced in this study. These test cases focus on simplified problems with known analytical solutions, allowing for a detailed comparison with FEM results to evaluate key features of the updated model.

Verification of the Longitudinal Tie-Ballast Resistance

Given:

A straight rail is subjected to constant axial point load $P_L = 1.0 \times 10^7\ N$ applied at the right end ($x = L$), and the left end ($x = 0$) is fixed, as shown in Figure 15. The rail parameters are as follows: $L = 10\ m$, $E = 2.06 \times 10^{11}\ N/m^2$, $A = 0.0172\ m^2$. The longitudinal tie-ballast resistance is defined by Equation (3) and (5), with $k_x = 1.0 \times 10^7\ N/m$, $\lambda_x = 1$, and $d_{tie} = 0.5\ m$. Note that k_x is intentionally set to an extremely large value, which is unrealistic but allows for a visible comparison to the rail's already high axial stiffness (EA).

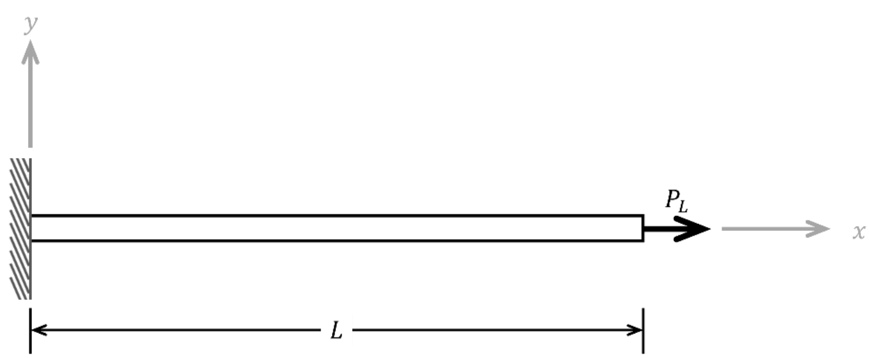

Figure 15 Depiction of the longitudinal tie-ballast resistance verification problem

Find:

The analytical axial displacement $u(x)$ along the rail and compare the results with the FEM simulation.

Solution:

From Table 1, the equations governing this problem are:

$$\frac{dP(x)}{dx} = \frac{\lambda_x\, k_x}{d_{tie}}\, u(x) \tag{97}$$

$$\frac{du(x)}{dx} = \frac{P(x)}{EA} \tag{98}$$

Combining the equations above yields:

$$\frac{d^2u(x)}{dx^2} - \alpha^2\, u(x) = 0 \tag{99}$$

where:

$$\alpha^2 = \frac{\lambda_x\, k_x}{E\ A\ d_{tie}} \tag{100}$$

The general solution to Equation (99) is:

$$u(x) = C_1\, cosh(\alpha x) + C_2\, sinh(\alpha x) \tag{101}$$

Using the given boundary conditions, $u(0) = 0$, and $P(L) = P_L$, the particular solution is:

$$u(x) = \frac{P_L}{E\ A\ \alpha\ cosh(\alpha L)}\, sinh(\alpha x) \tag{102}$$

A comparison of the analytical solution and the FEM results using 10 elements and 1 time-step is shown in Figure 16. The axial displacement values at $x = L$ differ by only 0.007%, demonstrating that the code accurately captures the longitudinal tie-ballast resistance effects under the given assumptions.

To illustrate the influence of longitudinal resistance, Equation (102) is compared with the case where $k_x = 0$. In this scenario, the displacement is:

$$u(x) = \frac{P_L}{EA}\,x \tag{103}$$

This linear equation is a standard result in basic solid mechanics textbooks and will not be derived here. The comparison between these cases is also plotted in Figure 16, highlighting the effect of longitudinal resistance.

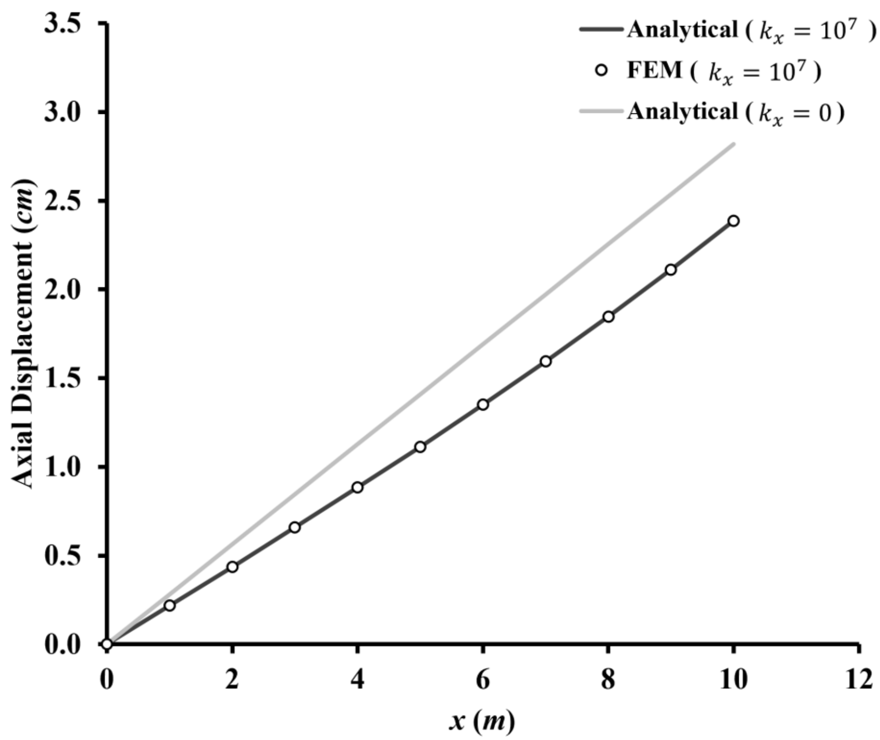

Figure 16 Comparison of analytical and FEM solutions for axial displacement under constant axial load when affected by longitudinal tie-ballast resistance

Verification of the Lateral Tie-Ballast Resistance

Although no analytical solution exists for comparison with the bilinear or trilinear lateral tie-ballast resistance formulations, the code can still be verified by making simplifying assumptions.

For instance, considering the compacted ballast condition, if the slopes of the first two segments of the piecewise function are set to the same value, the lateral displacements of the rail can be compared to results derived from the beams-on-elastic-foundations theory (Oden, 1967). Under these conditions, the mathematical formulations are equivalent, provided the lateral displacement values remain below the limit. This validation approach is demonstrated in the following example problem.

Given:

A straight rail is subjected to constant lateral point load $V_{y,0,5L} = 1.0 \times 10^5\ N$ applied at the midpoint, with both ends free to displace or rotate, as shown in Figure 17. The rail parameters are as follows: $L = 10\ m$, $E = 2.06 \times 10^{11}\ N/m^2$, $A = 0.0172\ m^2$, $I_{zz} = 1.22 \times 10^{-5}\ m^4$. The ballast is compacted, and the lateral tie-ballast resistance is defined by Equation (2) and (6), with $F_{y,pk} = 25000\ N$, $v_{pk} = 1\ m$, $F_{y,lt} = 50000\ N$, $v_{lt} = 2\ m$, $\lambda_y = 1$, and $d_{tie} = 0.5\ m$.

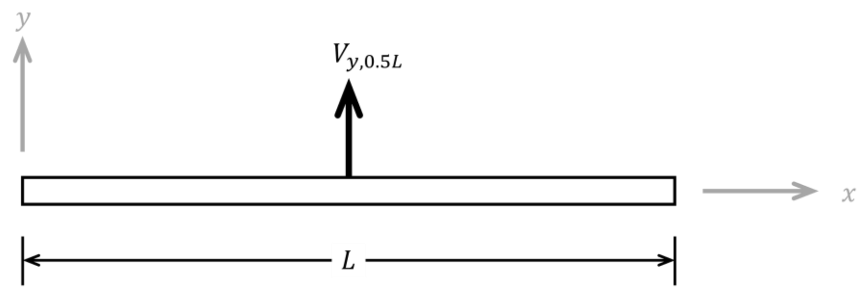

Figure 17 Depiction of the lateral tie-ballast resistance verification problem

Find:

The analytical lateral displacement $v(x)$ along the rail and compare the results with the FEM simulation.

Solution:

The resistance parameters are related as follows:

$$\frac{F_{y,pk}}{v_{pk}} = \frac{F_{y,lt} - F_{y,pk}}{v_{lt} - v_{pk}} = k_y \tag{104}$$

Here, k_y is the linear lateral tie-ballast resistance coefficient. Equation (6) can be simplified as:

$$f_y(v) = \begin{cases} -\dfrac{\lambda_y\, k_y}{d_{tie}}\ v, & |v| \le v_{lt} \\ \qquad\quad 0, & |v| > v_{lt} \end{cases} \tag{105}$$

It has the same mathematical form as Equation (7) for $|v| \le v_{lt}$.

Previously derived by Musu (2021), the vertical displacement of a beam resting on an elastic foundation subjected to a constant concentrated vertical load ($V_{z,0.5L}$) at midpoint can be expressed as:

$$w(x) = \delta_A \, cosh\big(\beta\ (L - x)\big)\, cos\big(\beta\ (L - x)\big) + \frac{\theta_A}{2\beta}\ \big(sinh\big(\beta\ (L - x)\big)\, cos\big(\beta\ (L - x)\big) + cosh\big(\beta\ (L - x)\big)\ sin\big(\beta(L - x)\big)\big) \tag{106}$$

where:

$$\beta = \sqrt[4]{\frac{k_z}{4\ E\ I_{yy}}} \tag{107}$$

$$\theta_A = -\delta_A\ \beta\ \left(tanh\left(\frac{\beta L}{2}\right) - tan\left(\frac{\beta L}{2}\right)\right) \tag{108}$$

$$\delta_A = \beta\ V_{z,0}\ \left\{k_z\ \left[sinh\left(\frac{\beta L}{2}\right) cos\left(\frac{\beta L}{2}\right) + cosh\left(\frac{\beta L}{2}\right) sin\left(\frac{\beta L}{2}\right) - \left(tanh\left(\frac{\beta L}{2}\right) - tan\left(\frac{\beta L}{2}\right)\right)\left(sinh\left(\frac{\beta L}{2}\right) sin\left(\frac{\beta L}{2}\right)\right)\right]\right\}^{-1} \tag{109}$$

By substituting k_z with $\frac{\lambda_y\, k_y}{d_{tie}}$, $V_{y,0.5L}$ with $V_{z,0.5L}$, and $w(x)$ with $v(x)$, the analytical solution for the problem can be obtained.

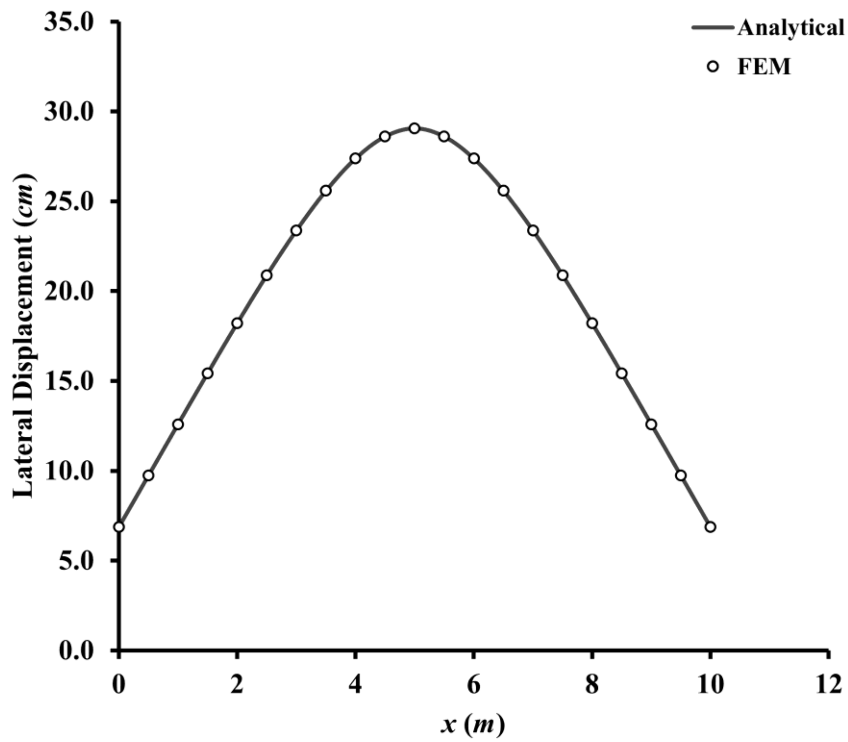

Figure 18 Comparison of analytical and FEM solutions for lateral displacement under constant lateral shear when affected by linear lateral tie-ballast resistance

As illustrated in Figure 18, the analytical solution aligns closely with the FEM simulation when using 20 elements and 1 time-step. The linear lateral tie-ballast resistance behaves similarly to an elastic foundation, effectively restraining the rail from displacing under the lateral shear load applied at the midpoint. As a result, the successful comparison confirms the correct implementation of the method in the computational code.

Verification of the Displacement-Control Algorithm

As the force-control algorithm has already been established as reliable, the displacement-control algorithm is verified by comparing its results with those obtained using the force-control algorithm for buckling cases with known analytical solutions. For simplicity in deriving the analytical solution, the linear strain-displacement relationship is used in the verification process. This is also achievable in the code, with a flag allowing the user to switch between the linear and nonlinear strain-displacement relationships.

Given:

A rail is subjected to an axial point load P applied at left end $(x = 0)$. Both ends are simply supported but axial displacements are permitted at $x = 0$, as illustrated in Figure 19. The rail parameters are as follows: $L = 10\ m$, $E = 2.06 \times 10^{11}\ N/m^2$, $A = 0.0172\ m^2$, $I_{zz} = 1.22 \times 10^{-5}\ m^4$. Tie-ballast resistances and the fastener rotational resistance are neglected for this specific case.

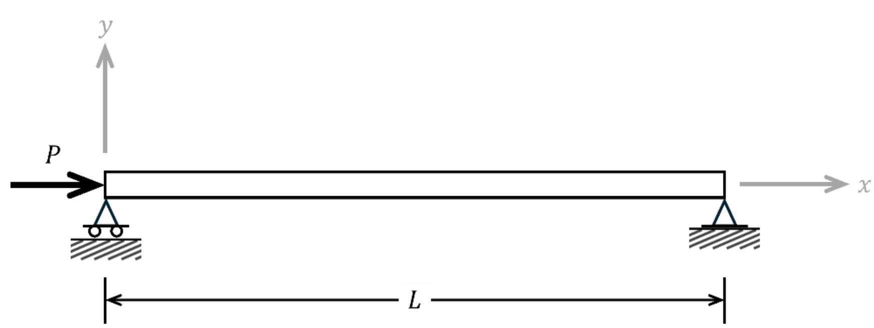

Figure 19 Depiction of the displacement-control algorithm verification problem

Find:

The analytical lateral buckling load of the rail and compare the results with the FEM simulations using both the force-control and displacement-control algorithms.

Solution:

The analytical solution to this problem is the well-known Euler-buckling formula for a pinned-end column (Allen and Haisler, 1985):

$$P_{cr} = \frac{\pi^2 \, E \, I_{zz}}{L^2} \tag{110}$$

Here, P_{cr} is the critical buckling load, which evaluates to $P_{cr} = 248.8 \, KN$.

To obtain the FEM solution, initial geometric imperfections are introduced to the rail to account for geometric nonlinearity effects. This is done by applying a small lateral load at the midpoint, ensuring the misalignment remains minor enough to not influence the buckling load significantly.

For both simulations, the rail is divided into 20 elements. The results are presented in Figure 20, demonstrating that both algorithms converge to a buckling load consistent with the analytical solution. Furthermore, the load vs. maximum displacement curves for the two solving methods show remarkable similarity.

Thus, the displacement-control algorithm is verified and deemed suitable for buckling simulations.

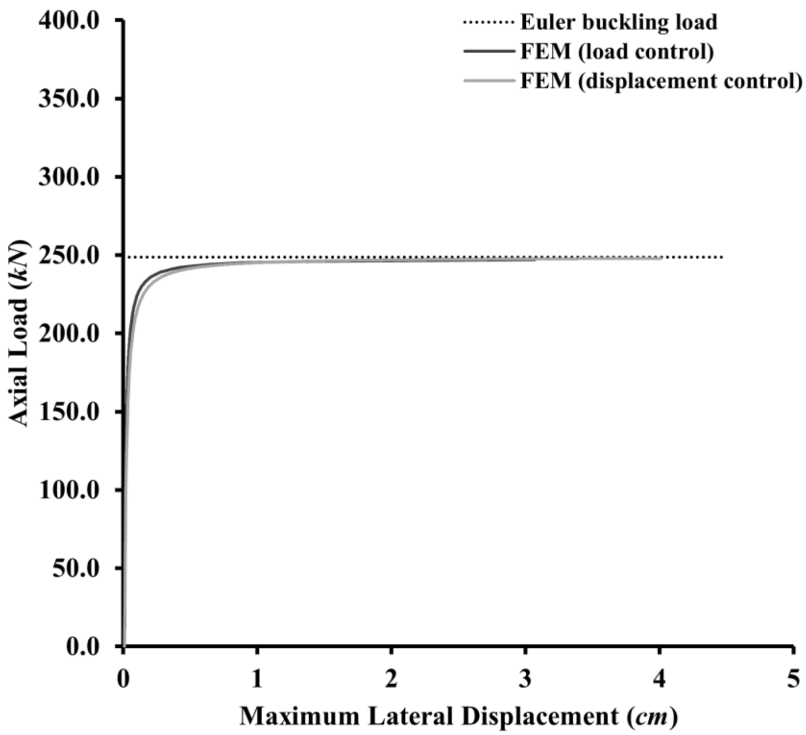

Figure 20 Result of the applied axial load vs. maximum displacement curves for different solving procedures

CHAPTER IV

RESULTS

This chapter employs the developed finite element model to conduct sensitivity studies on rail buckling. Various factors influencing the buckling load are analyzed, including material properties, rail geometry, track modulus, fastener stiffness, and tie-ballast resistance. The sensitivity of these parameters is compared to identify the most critical factors affecting rail buckling behavior.

A general base case is simulated, with each sensitivity study modifying one input parameter at a time. The International System of Units (SI) is used throughout this research, and conversions between SI units and imperial units are provided in Appendix B. Buckling simulations are performed on a constrained rail section of length L, where axial contraction is permitted while all other displacements and rotations are restricted at both ends. To induce buckling, mechanical axial loads are applied at both ends, as illustrated in Figure 21. These loads are assumed to be equivalent to thermal loads resulting from temperature changes relative to the RNT, as determined by Equation (17).

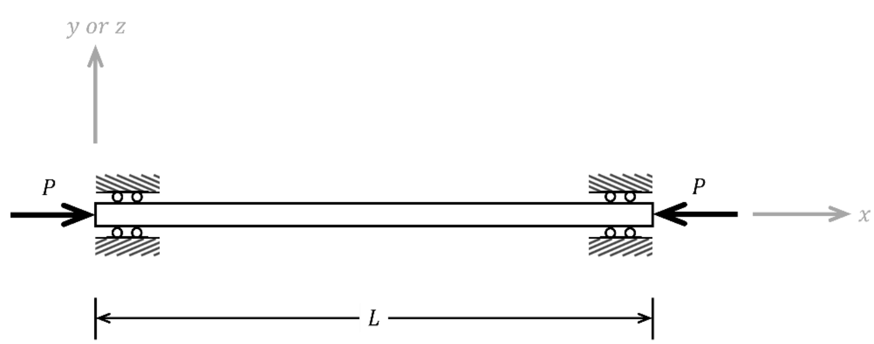

Figure 21 Boundary conditions for a rail buckling problem

Due to the symmetry of the boundary conditions along the axial direction, the problem complexity can be reduced. By simulating only half of the rail buckle length and allowing lateral and vertical displacements at $x = L/2$ while restricting axial displacements and rotations, the required number of elements is halved without affecting the results. This simplified boundary condition setup is illustrated in Figure 22.

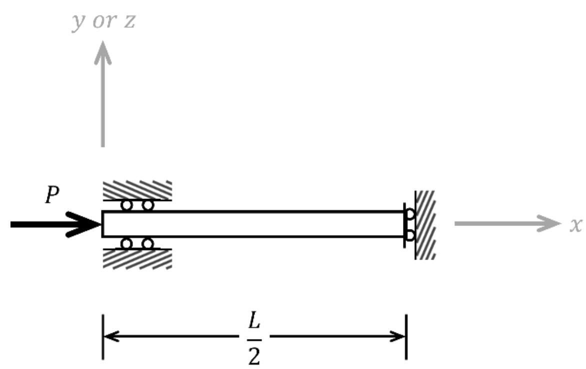

Figure 22 Boundary conditions applied in this research

Initial lateral geometric imperfections, or misalignments, are also considered in the following cases, as secondary moments would be zero for a perfectly aligned rail. The misalignment shape is generated by applying a lateral point load at $x = L/2$. This process can be performed using either the force-control or displacement-control algorithm. After the misalignment process, the displacement values used for tie-ballast resistance effects are reset to zero. This reset assumes the rail is at rest when buckling is initiated, indicating that the misalignment occurred prior to buckling.

To ensure realistic buckling results, the geometry parameters are based on the AREMA 136RE rail head section, including the moments of inertia in both directions and the rail cross-sectional area. Additionally, the material properties of steel are estimated according to industry specifications (Nippon Steel Corporation, 2020; Musu, 2021). Since the system consists of two aligned rails, geometric parameters, such as the cross-sectional area, are doubled before being applied to the model. Unless otherwise specified, the ballast condition is assumed to be disturbed. In this case, the lateral tie-ballast resistance curve can be fully characterized by the limit force value and its corresponding lateral displacement. A complete list of input parameters is provided in Table 2 and Table 3, expressed in SI units and imperial units, respectively. While these parameters are designed to approximate realistic conditions, they may vary and are intended primarily to demonstrate the capabilities of the code.

Table 2 Base case input parameters for the sensitivity study (SI units)

Input Parameter	**Value**	**Unit**
Rail Buckling Length, L	10.00	m
Cross-Section, $2A$	1.72×10^{-2}	m^2
Moment of Inertia, $2I_{yy}$	7.90×10^{-5}	m^4
Moment of Inertia, $2I_{zz}$	1.22×10^{-5}	m^4
Rail Weight Per Unit Length, $2n_{rail}$	1.32×10^{3}	N/m
Modeled Tie-Weight, N_{tie}	1.00×10^{3}	N
Modeled Friction Coefficient, μ	1.50	
Rail Young's Modulus, E	2.06×10^{11}	N/m^2
Rail Thermal Expansion Coefficient, α	1.05×10^{-5}	1/℃
Tie-Spacing, d_{tie}	0.50	m
Longitudinal Tie-Ballast Resistance Coefficient, k_x	2.00×10^{6}	N/m
STPT Limit Lateral Force, $F_{y,lt}$	1.00×10^{4}	N
STPT Limit Lateral Displacement, v_{lt}	5.00×10^{-3}	m
Track Modulus, k_z	7.00×10^{7}	N/m^2
Fastener Rotational Stiffness, S	2.25×10^{5}	$N \cdot m/rad$
STPT Tie-Weight, $N_{tie,STPT}$	1.00×10^{3}	N
STPT Friction Coefficient, μ_{STPT}	1.50	
Misalignment Value, d_{mis}	4.00×10^{-2}	m

Table 3 Base case input parameters for the sensitivity study (imperial units)

Input Parameter	**Value**	**Unit**
Rail Buckling Length, L	393.70	in
Cross-Section, $2A$	26.66	in^2
Moment of Inertia, $2I_{yy}$	189.80	in^4
Moment of Inertia, $2I_{zz}$	29.27	in^4
Rail Weight Per Unit Length, $2n_{rail}$	7.54	lbf/in
Modeled Tie-Weight, N_{tie}	224.81	lbf
Modeled Friction Coefficient, μ	1.50	
Rail Young's Modulus, E	2.99×10^7	psi
Rail Thermal Expansion Coefficient, α	5.83×10^{-6}	1/°F
Tie-Spacing, d_{tie}	19.69	in
Longitudinal Tie-Ballast Resistance Coefficient, k_x	11420.37	lbf/in
STPT Limit Lateral Force, $F_{y,lt}$	2248.10	lbf
STPT Limit Lateral Displacement, v_{lt}	0.20	in
Track Modulus, k_z	10152.73	psi
Fastener Rotational Stiffness, S	1.99×10^6	$lbf \cdot in/rad$
STPT Tie-Weight, $N_{tie,STPT}$	224.81	lbf
STPT Friction Coefficient, μ_{STPT}	1.50	
Misalignment Value, d_{mis}	1.57	in

Mesh and Step Size Convergence Studies

The displacement-control algorithm is employed throughout the sensitivity study. Convergence studies are conducted for the entire buckling process, with axial load applied at $x = 0$. The buckling load values are analyzed for varying mesh densities and displacement step sizes. The step size is initially set to a small value to ensure accuracy during the mesh convergence study. Once the optimal mesh size is determined, the step size is chosen by verifying convergence with increasing step sizes.

Mesh Convergence Study

The step size is initially set to $2 \times 10^{-4}\ m$, and this value remains the same throughout the misalignment and buckling process. Only uniform meshes are considered, with the number of elements ranging from 10 to 80. The load vs. displacement curves for different cases are presented in Figure 23.

The differences in the minimum buckling loads (P_{min}) and the corresponding lateral displacements (v_{min}) for each case are compared with the results from the finest mesh, as shown in Figure 24. The results demonstrate a clear convergence trend in both parameters as the number of elements increases. The differences for both parameters between 40 and 80 elements are under 2%, indicating sufficient convergence. Based on these findings, the corresponding element length, $0.25\ m$, is selected for subsequent simulations, and 40 elements will be used for all cases unless L is modified.

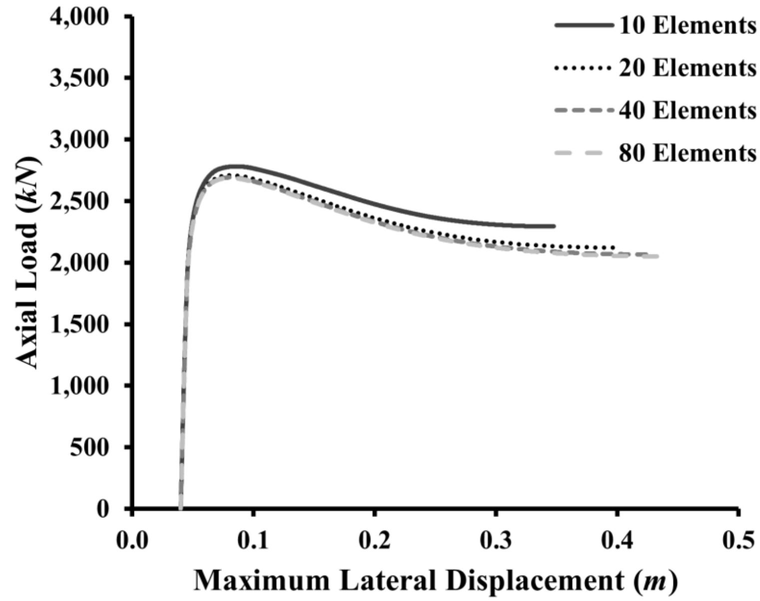

Figure 23 Maximum lateral displacement vs. applied axial load curves for the mesh convergence study

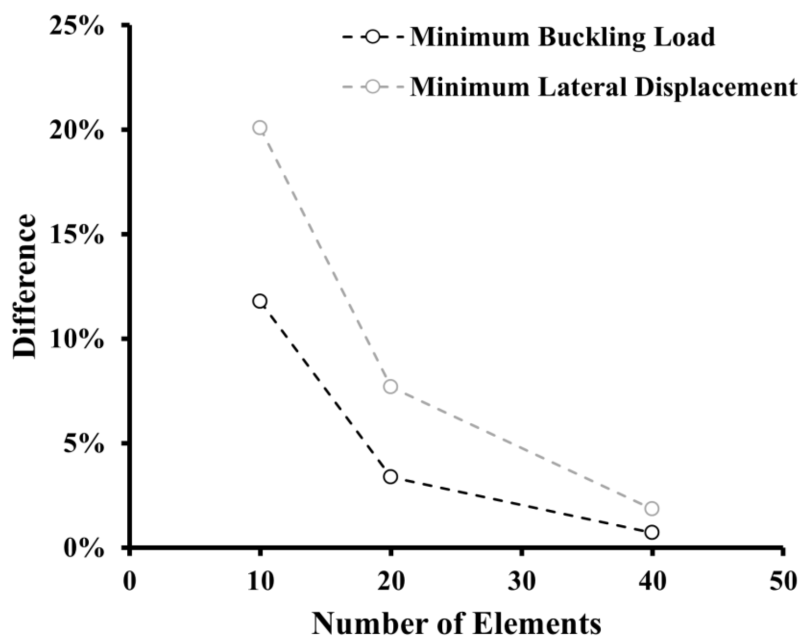

Figure 24 Convergence of minimum buckling load and corresponding lateral displacement relative to the finest mesh

Step Size Convergence Study

With 40 elements selected based on previous simulations, various larger step sizes are tested and compared. The results, shown in Figure 25, indicate that when the step size is set to $8 \times 10^{-4}\ m$, the difference from the smallest step size ($2 \times 10^{-4}\ m$) for both P_{min} and v_{min} is under 2%. Therefore, a step size of $8 \times 10^{-4}\ m$ is deemed sufficient and will be used in the sensitivity study.

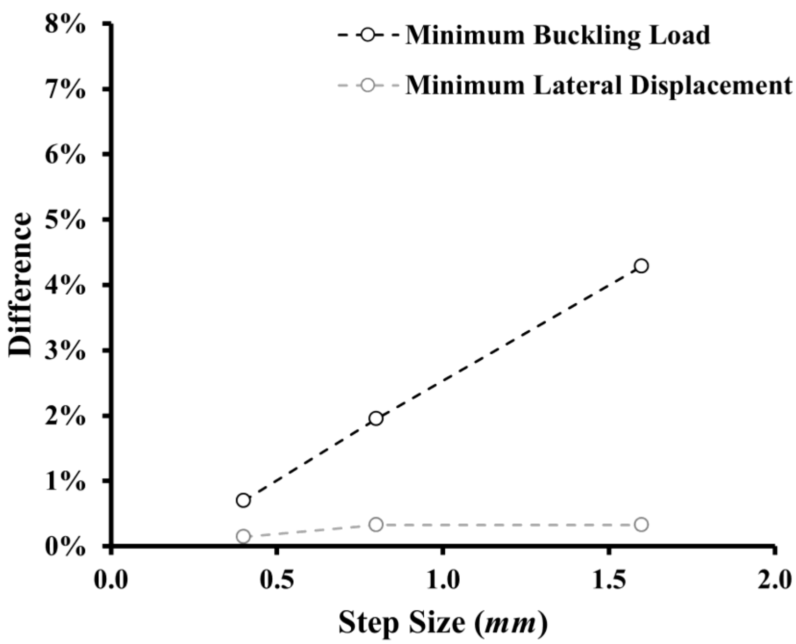

Figure 25 Convergence of minimum buckling load and corresponding lateral displacement relative to the finest step size

Sensitivity Study of Rail Misalignment

Misalignment values (d_{tie}) varied from $0.02\ m$ to $0.06\ m$. Although additional force is required to deform the rail into its initial misaligned configuration, as illustrated in Figure 26, this process is assumed to have been completed beforehand and is not considered in the calculation of the buckling load.

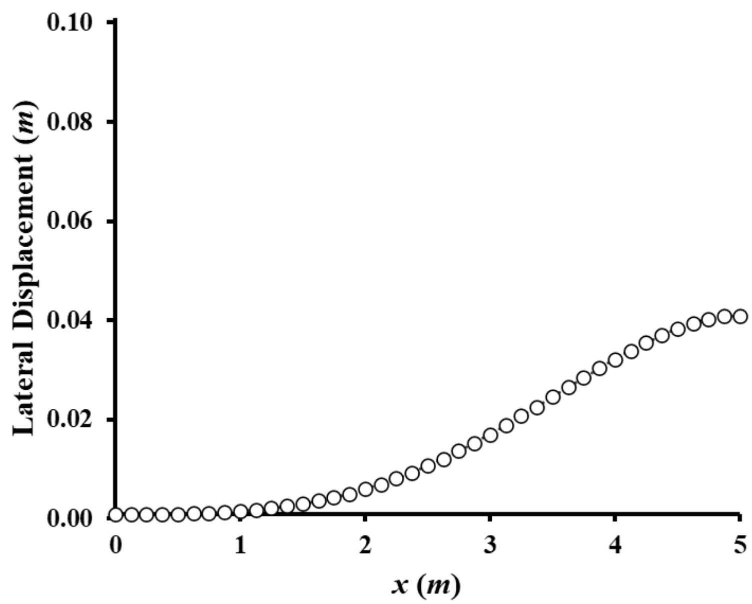

Figure 26 Illustration of the lateral displacements along the rail when it is misaligned

The results for each case are presented in Figure 27 and Figure 28. P_{min} is observed to be relatively insensitive to d_{tie}. However, the critical buckling load (P_{cr}) exhibits a high sensitivity to small initial misalignments, converging to a lower value as d_{tie} increases. This highlights the practical importance of even small geometric imperfections: while a perfectly aligned track can sustain extremely high buckling load, P_{cr} drops significantly—by 22.5%—when d_{tie} increases from $0.02\ m$ to $0.04\ m$.

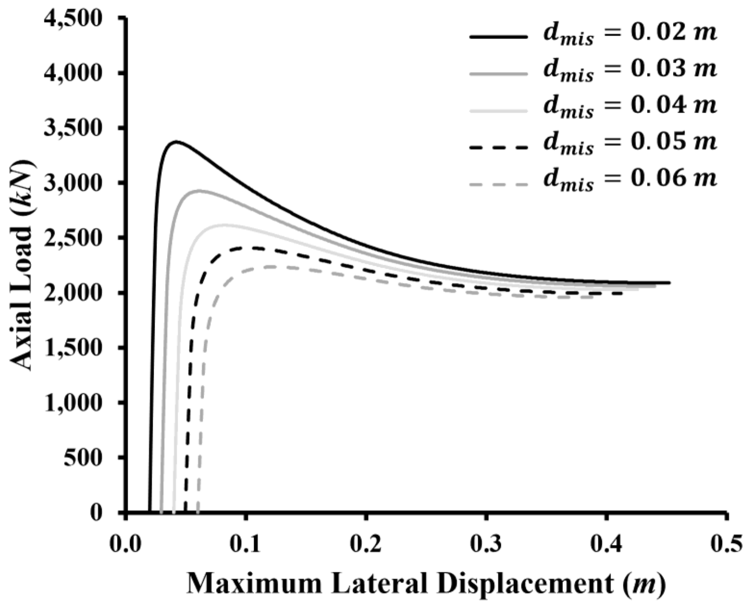

Figure 27 Maximum lateral displacement vs. applied axial load with various misalignment values applied to a typical rail structure

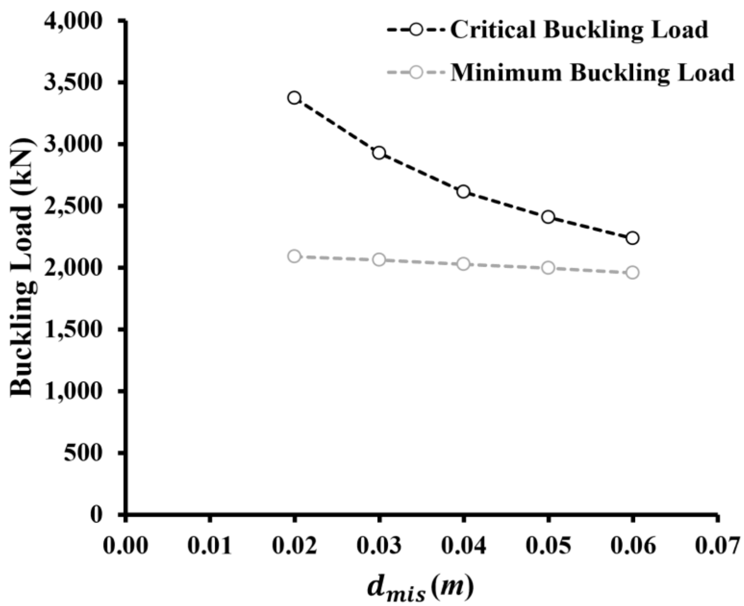

Figure 28 Predicted effect of misalignment value change on buckling load of a typical rail structure

Sensitivity Study of the Longitudinal Tie-Ballast Resistance

The effect of the longitudinal tie-ballast resistance (hereafter referred to as the longitudinal resistance) is analyzed by varying the resistance coefficient (k_x), with the results shown in Figure 29 and Figure 30.

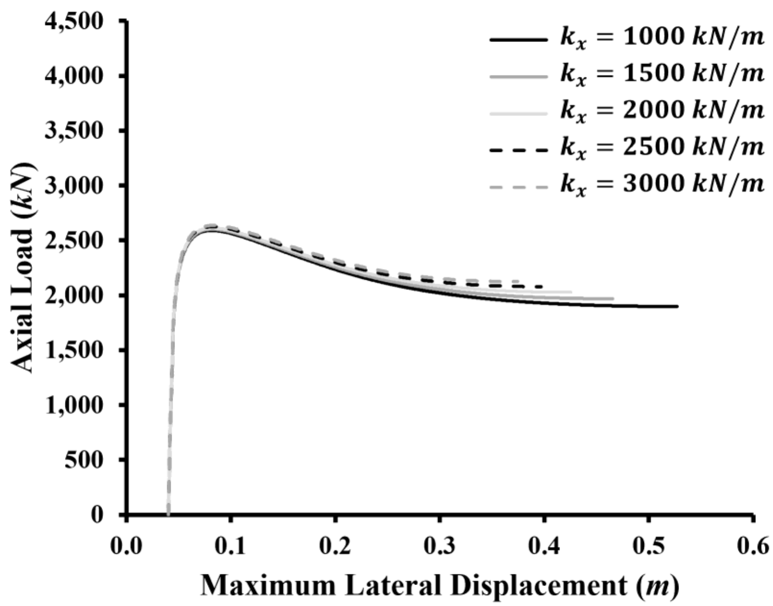

Figure 29 Maximum lateral displacement vs. applied axial load with various longitudinal tie-ballast resistance coefficients applied to a typical rail structure

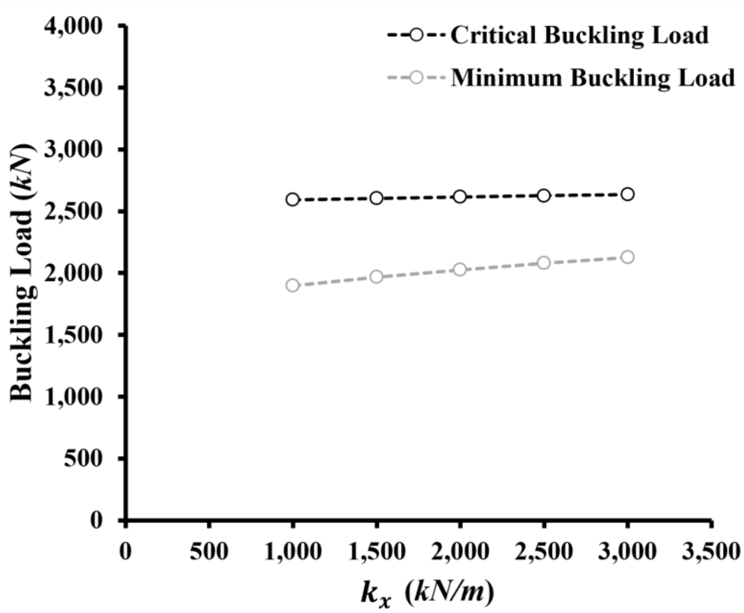

Figure 30 Predicted effect of longitudinal tie-ballast resistance coefficient change on buckling load of a typical rail structure

As the rail's axial stiffness (EA) is large, it dominates the axial displacements before the critical buckling point. Consequently, the axial displacements remain small, as shown in Figure 31, and the longitudinal resistance has negligible influence on the critical buckling load. However, after the critical buckling point, the rail structure softens, leading to rapid increases in axial displacement. At these larger displacement values, the longitudinal resistance becomes significant, and higher k_x result in increased P_{min}. This indicates that, although the longitudinal resistance has minimal impact on P_{cr}, it remains a crucial factor in rail buckling analysis. Its presence helps mitigate buckling risks when additional energy is introduced to the system, such as from trains passing through.

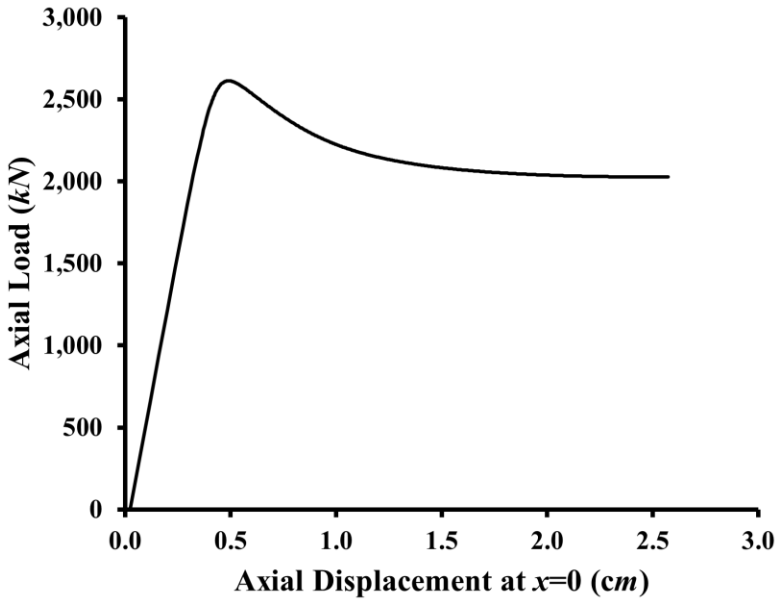

Figure 31 Demonstration of the axial displacement change of a rail when axial load is applied

Sensitivity Study of the Lateral Tie-Ballast Resistance

As the lateral tie-ballast resistance (hereafter referred to as the lateral resistance) is highly nonlinear, three different scenarios are examined. The first two cases assume a disturbed ballast condition, where the lateral resistance curve is characterized by two parameters: the limit force of the resistance curve ($F_{y,lt}$) and the corresponding lateral displacement (v_{lt}). The third case assumes a compacted ballast condition, introducing two additional parameters: the peak force of the resistance curve ($F_{y,pk}$) and the corresponding lateral displacement (v_{pk}).

First Case: Variation in Limit Force

For the first scenario, $F_{y,lt}$ is varied from $5\ kN$ to $15\ kN$, and the results are presented in Figures 32 and 33. The findings demonstrate that $F_{y,lt}$ is a critical factor in rail buckling, significantly influencing both P_{cr} and P_{min}. The trend reveals that at lower $F_{y,lt}$ values, the difference between the P_{cr} and P_{min} diminishes. This corresponds to previous research findings (Samavedam et al., 1993; Kish and Samavedam, 2013), suggesting that when the lateral resistance is weak, softening may not occur, and progressive buckling dominates. However, while the snap-through phenomenon is less likely in such cases, P_{cr} remains significantly reduced, highlighting the importance of avoiding such conditions.

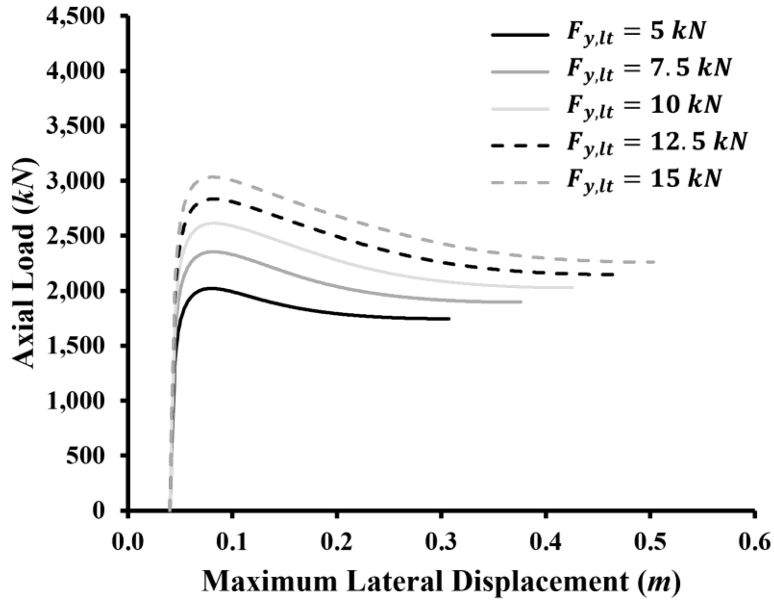

Figure 32 Maximum lateral displacement vs. applied axial load with various limit lateral resistance values applied to a typical rail structure

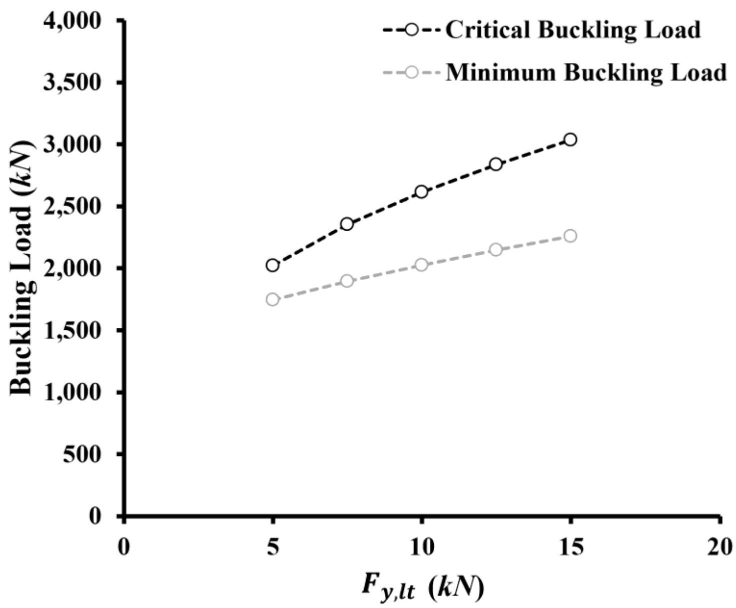

Figure 33 Predicted effect of changes in the limit lateral resistance value on buckling load of a typical rail structure

Second Case: Variation in Limit Displacement

For the second scenario, v_{lt} is varied from $0.25\ cm$ to $0.75\ cm$, with the results shown in Figures 34 and 35. The results indicate that v_{lt} has minimal impact on both P_{cr} and P_{min}, only slightly altering the initial slope of the load-displacement curve. In practical STPT experiments, accurately capturing v_{lt} may be challenging. However, the results suggest that $F_{y,lt}$ is a more influential parameter affecting the buckling load and should be prioritized in analyses.

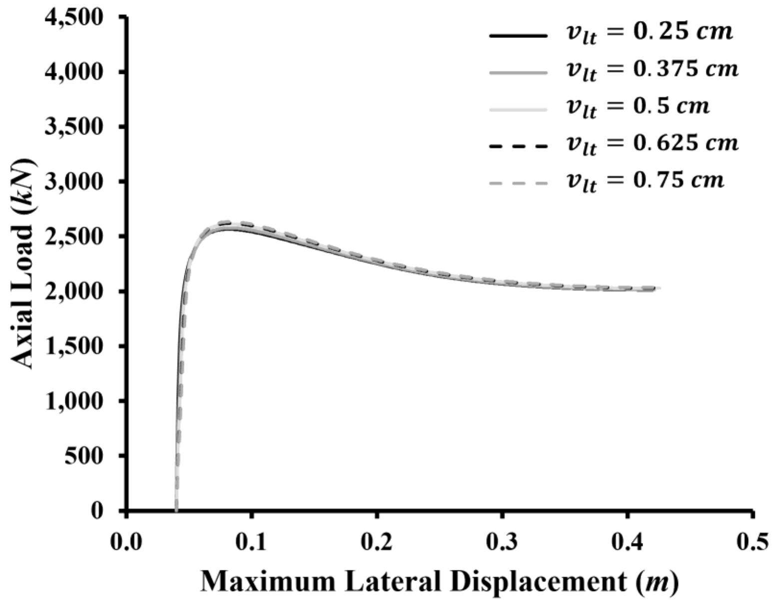

Figure 34 Maximum lateral displacement vs. applied axial load with various limit lateral displacement values applied to a typical rail structure

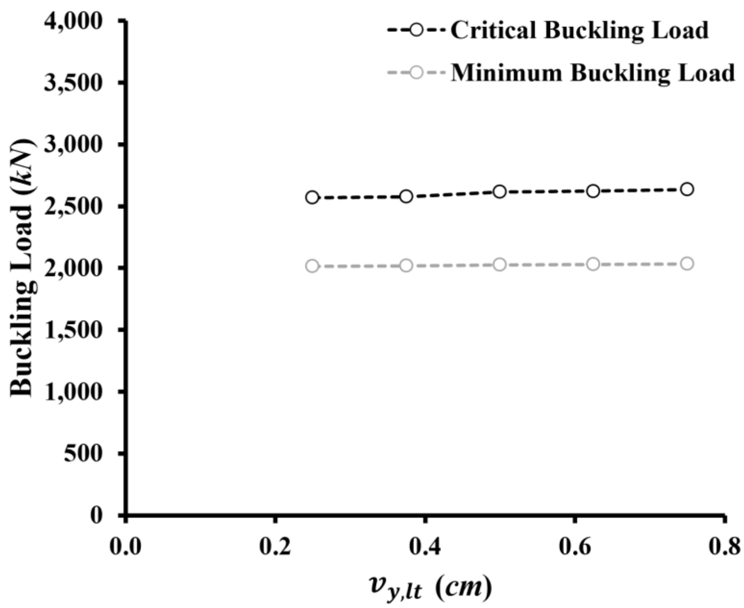

Figure 35 Predicted effect of changes in the limit lateral displacement value on buckling load of a typical rail structure

Third Case: Compacted Ballast Condition

In the third scenario, the trilinear resistance curve is applied to simulate the compacted ballast condition. $F_{y,pk}$ is varied from $10\ kN$ to $20\ kN$, while the other parameters are fixed as $v_{pk} = 0.5\ cm$, $F_{y,lt} = 10\ kN$, and $v_{lt} = 5\ cm$. Note that the first case can be simplified as the disturbed ballast condition, where $F_{y,pk} = F_{y,lt}$. The results, shown in Figures 36 and 37, indicate that $F_{y,pk}$ strongly affects P_{cr}.

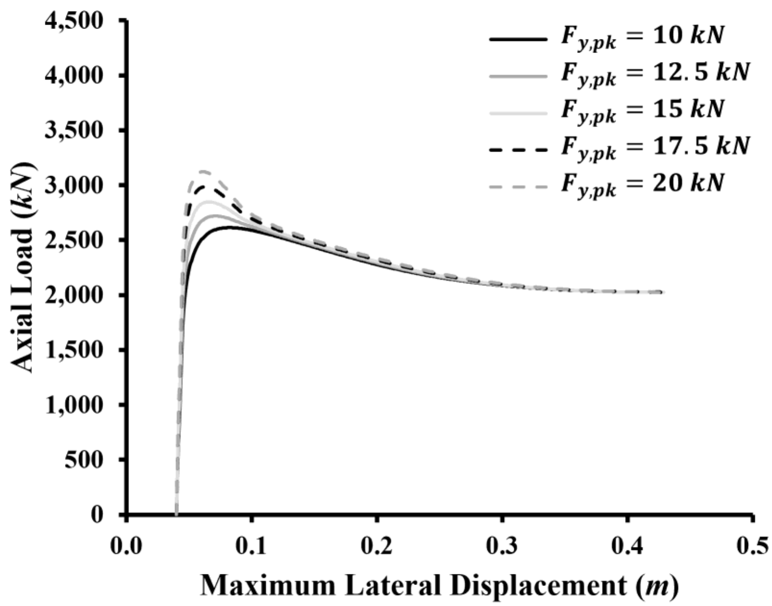

Figure 36 Maximum lateral displacement vs. applied axial load with various peak lateral resistance values applied to a typical rail structure

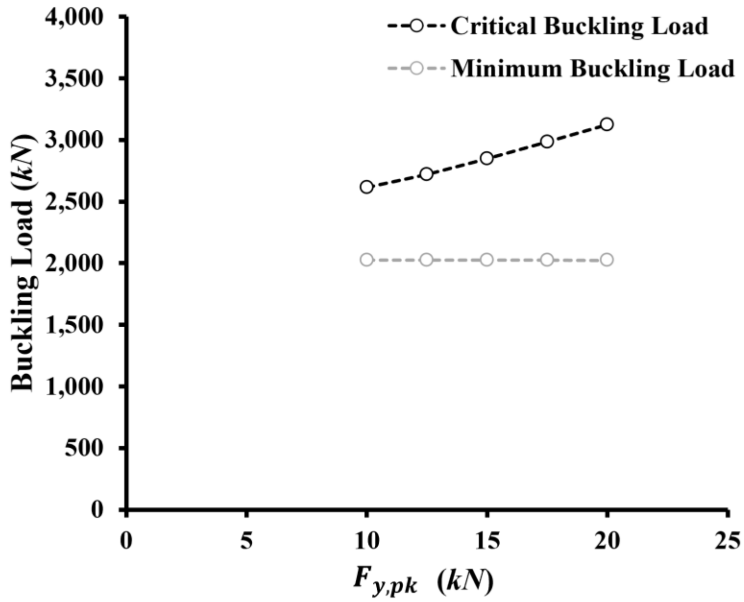

Figure 37 Predicted effect of changes in the peak lateral resistance value on buckling load of a typical rail structure

Comparing with previous results, it can be observed that for a compacted ballast condition ($F_{y,pk} = F_1$ and $F_{y,lt} = F_2$), the critical buckling load falls between those for disturbed ballast cases where $F_{y,lt} = F_1$ and $F_{y,lt} = F_2$, shown in Figure 38. This relationship provides a useful estimation method for P_{cr} with fewer simulations needed. Additionally, the P_{min} is less sensitive to changes in $F_{y,pk}$, provided $F_{y,lt}$ and v_{lt} remain constant.

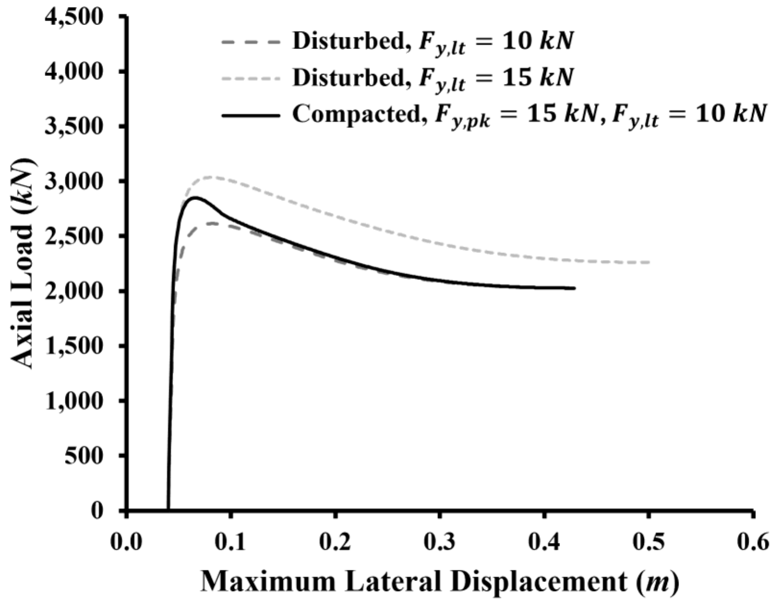

Figure 38 Maximum lateral displacement vs. applied axial load curve comparison between different ballast conditions

Sensitivity Study of the Fastener Rotational Resistance

The sensitivity of rail buckling to fastener rotational resistance is analyzed by varying the rotational stiffness (S) between $112.5\ kN \cdot m/rad$ to $337.5\ kN \cdot m/rad$. Figures 39 and 40 show the results. The initial slope of the load-displacement curve remains consistent across different values of S. However, as S increases, both the P_{cr} and P_{min} exhibit a linear increasing trend within the tested range, demonstrating the significant role of fastener rotational resistance in enhancing rail buckling stability.

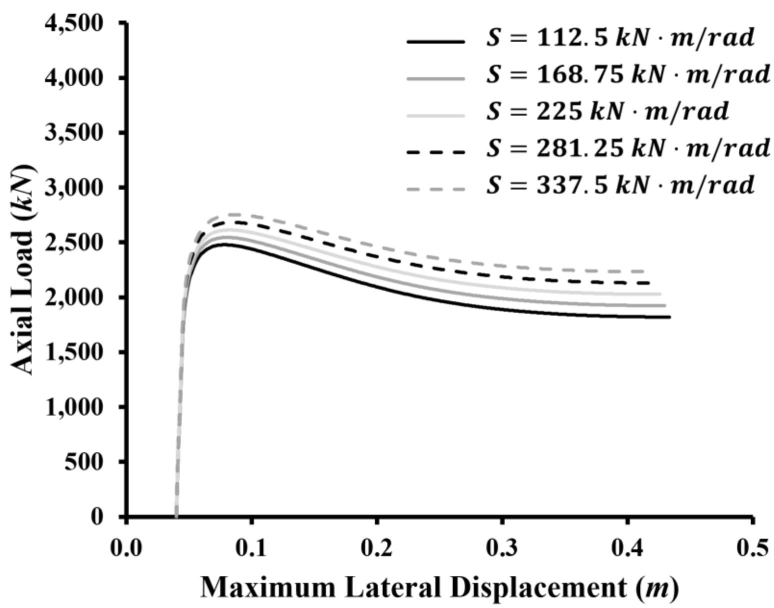

Figure 39 Maximum lateral displacement vs. applied axial load with various rotational stiffness values applied to a typical rail structure

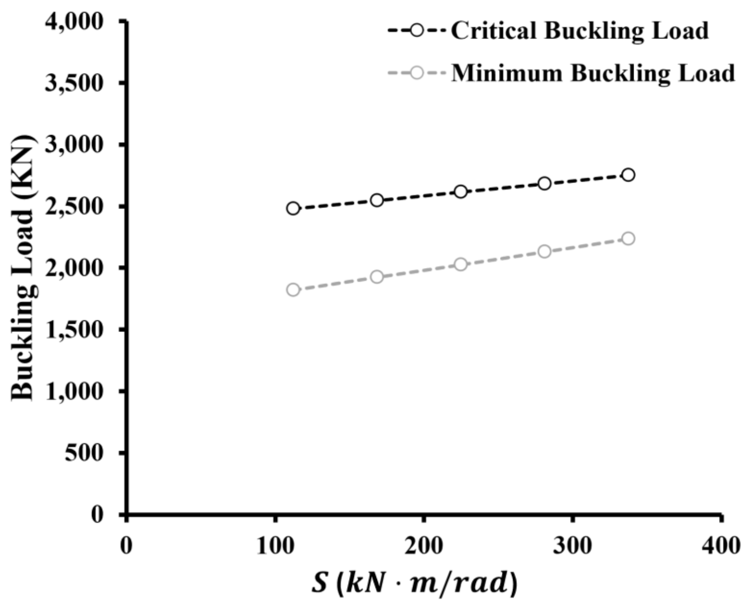

Figure 40 Predicted effect of rotational stiffness value change on buckling load of a typical rail structure

The effect of broken spikes (fasteners) was also examined in this study. Spikes, which are critical components connecting rails to ties, contribute significantly to providing rotational resistance. However, when spikes fail or are improperly installed, they lose their ability to provide rotational resistance.

In this model, the rotational resistance is represented as distributed moments along the rail. To simulate the failure of spikes, the stiffness matrix was modified element-wise to reflect the loss of rotational resistance over specific rail sections. It was further assumed that all spikes connecting a single tie to the rail fail simultaneously. Failures were distributed symmetrically on either side of the constrained rail section, beginning from the center. It is further assumed that the longitudinal and lateral resistance remain unaffected, as the main focus of the sensitivity study is to analyze the discontinuous distribution of the rotational resistance effect.

The results, shown in Figures 41 and 42, indicate that the failure of a small number of spikes has a negligible effect on rail buckling loads. Noticeable reductions in buckling loads are only observed when a continuous series of spikes fails, a scenario that is unlikely under normal operating conditions. Thus, based on the assumptions used in this study, broken spikes are not expected to critically influence rail buckling loads in most practical situations.

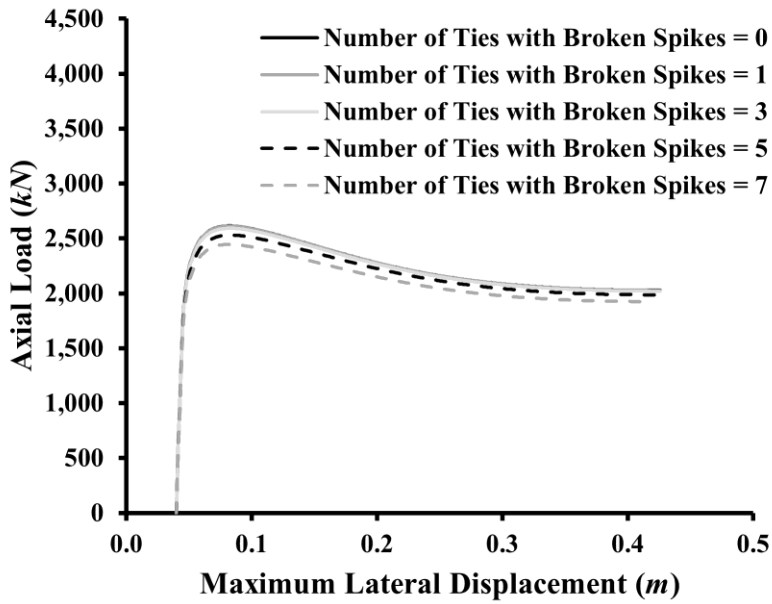

Figure 41 Maximum lateral displacement vs. applied axial load with various numbers of ties with broken spikes applied to a typical rail structure

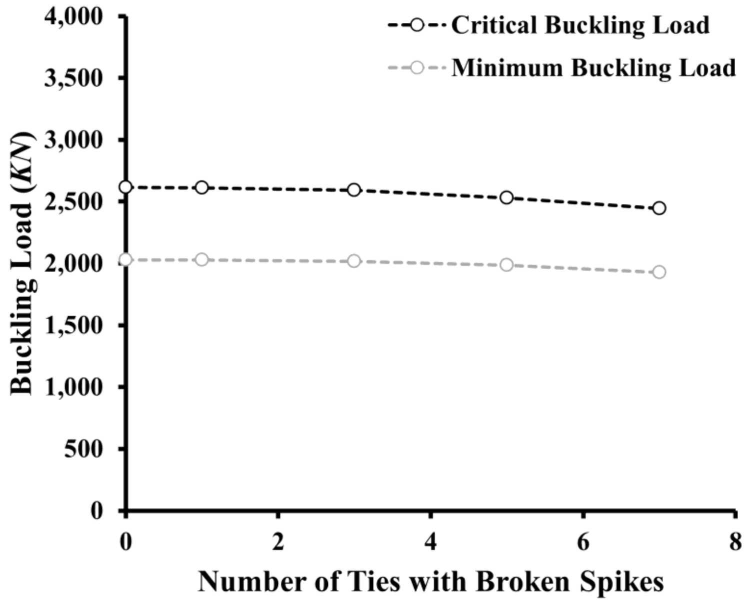

Figure 42 Predicted effect of numbers of ties with broken spikes change on buckling load of a typical rail structure

Sensitivity Study of the Rail Buckling Length

The constrained length (L) is a critical factor in rail buckling behavior. In the FEM model presented herein, L is a predefined value, making the selection of an appropriate L extremely important. The results for varying L are shown in Figures 41 and 42. It should be noted that for Figure 42, results are excluded for $L = 5\ m$ and $L = 7.5\ m$, as no clear buckling point is identified based on the defined criteria.

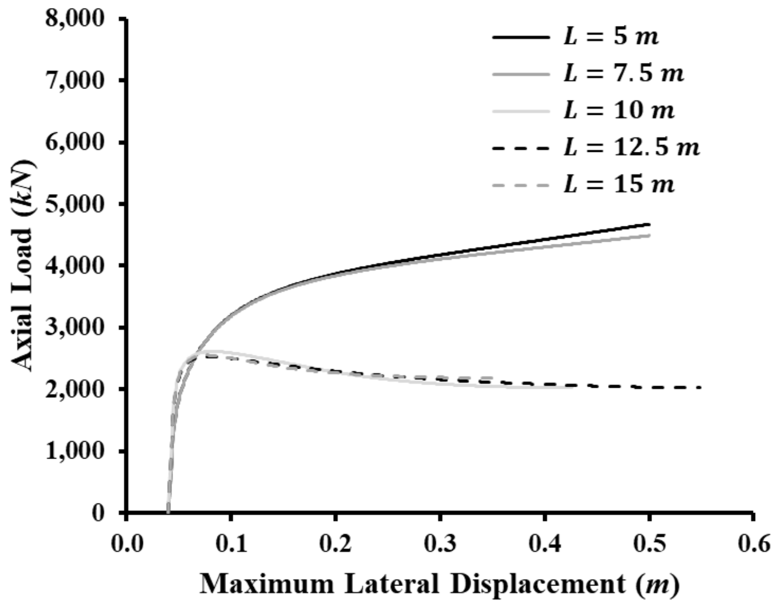

Figure 43 Maximum lateral displacement vs. applied axial load with various buckling length values applied to a typical rail structure

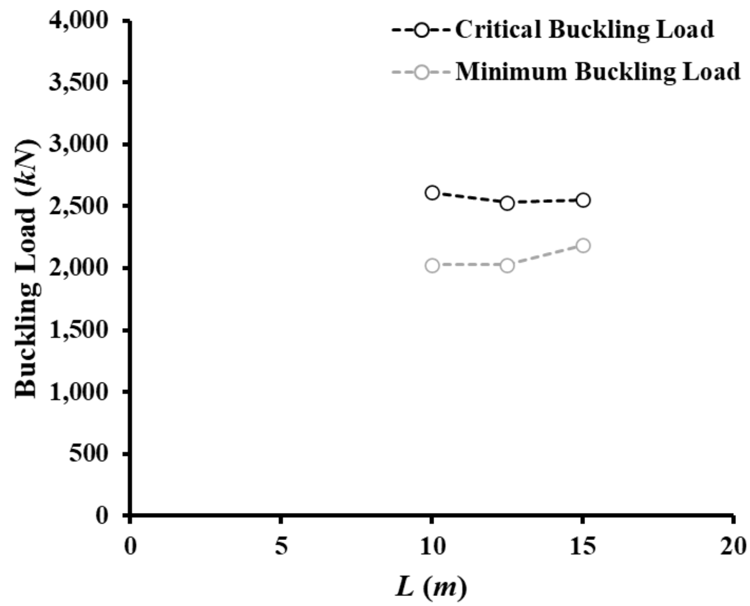

Figure 44 Predicted effect of buckling length change on buckling load of a typical rail structure

For small L values, no distinct instability point is observed, and the system exhibits higher overall stiffness compared to cases with larger L. However, softening still occurs, and rapid deformation may happen if sufficient axial load is applied. In real-world scenarios, a strictly constrained length may not exist, and when a certain axial load is reached, the rail could buckle with a larger buckling length.

The results also show that for sufficiently large L values, there is minimal difference in the buckling load. This suggests that once L exceeds a certain critical value, the buckling load becomes less sensitive to further increases in L.

Figures 41 and 42 illustrate these findings, highlighting the importance of selecting an appropriate L for accurate modeling and realistic rail buckling simulations.

Sensitivity Study of Multi-Influential Factors

Factors such as the friction coefficient of the tie-ballast interface (μ), tie-weight (N_{tie}), and tie-spacing (d_{tie}) influence multiple aspects of rail mechanics simultaneously. For instance, as shown in Equations (4),(5), and (6), all three factors impact both the longitudinal and lateral resistance, while d_{tie} also affects the rotational resistance, as indicated in Equations (4), (5), (6), and (9). Sensitivity studies are performed by varying these factors.

The effect of μ and w_{tie} are directly related. Results of varying these factors are presented herein. For the base case, according to Coulomb's friction law, w_{tie} contributes 15% of the total lateral resistance. This indicates that while w_{tie} does influence the buckling load, its effect is relatively limited, as shown in Figure 45 and Figure 46.

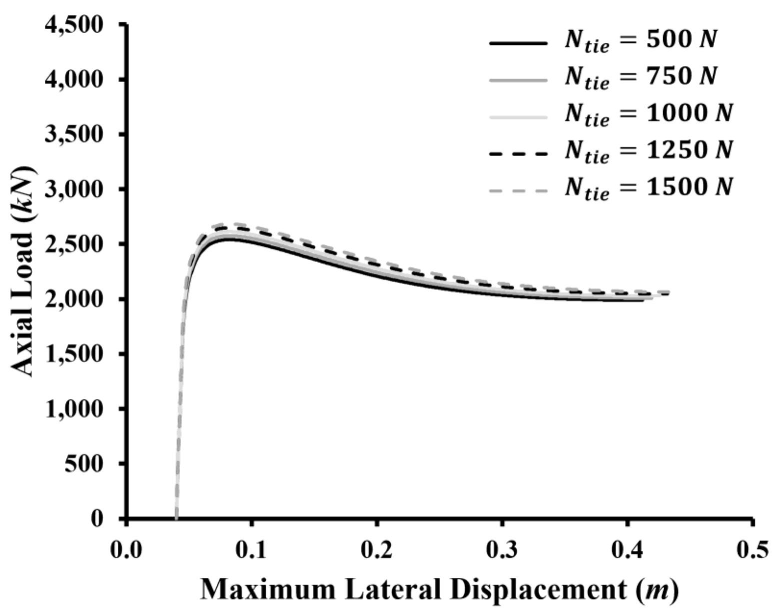

Figure 45 Maximum lateral displacement vs. applied axial load with various tie weight values applied to a typical rail structure

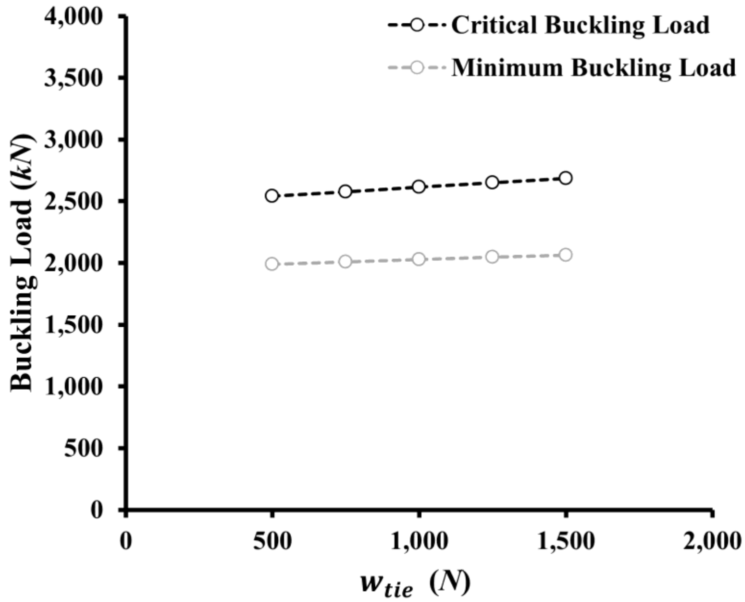

Figure 46 Predicted effect of tie weight value change on buckling load of a typical rail structure

In contrast, μ also impacts the lateral resistance contributed by rail weight and other normal forces, such as train weight. This also shows agreement with the results presented in Figure 47 and Figure 48, demonstrating a more sensitive trend as μ varies.

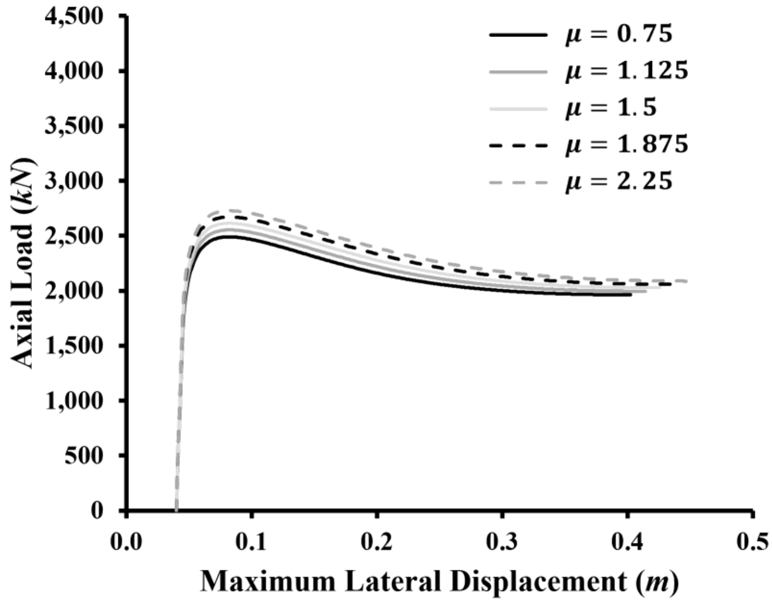

Figure 47 Maximum lateral displacement vs. applied axial load with various friction coefficient values applied to a typical rail structure

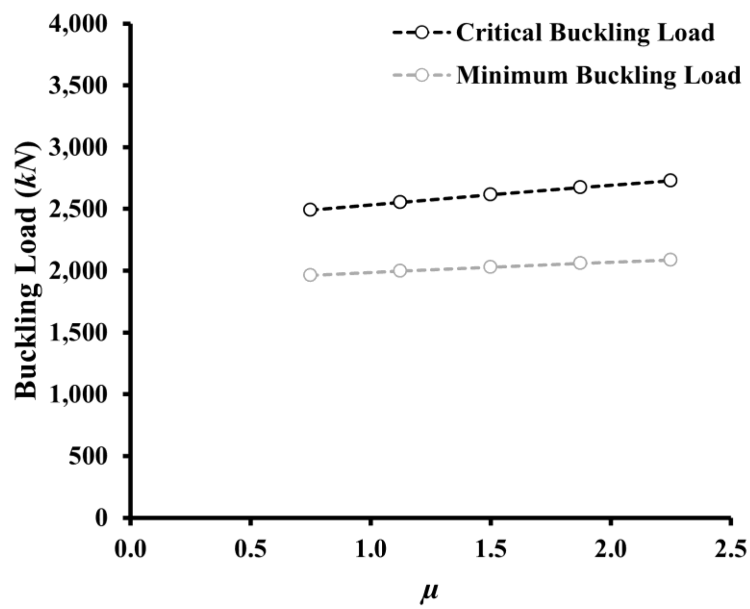

Figure 48 Predicted effect of friction coefficient value change on buckling load of a typical rail structure

In addition, while N_{tie} is less variable in daily use, μ can change due to environmental factors and tie conditions. For instance, μ may vary under different weather conditions, such as rain or mud accumulation. The model presented in this research demonstrates the potential effects of μ and provides a framework for conducting further, more detailed studies once more data becomes available for this parameter.

For d_{tie}, typical values in the United States are approximately 19.5 inches ($0.50\ m$) for wooden ties and 24 inches ($0.61\ m$) for concrete ties. Sensitivity tests explore a range of d_{tie} values spanning these standards. In this model, doubling d_{tie} effectively doubles the lateral, longitudinal, and rotational resistance, indicating a substantial impact on the rail buckling load, as shown in Figure 49 and Figure 50:

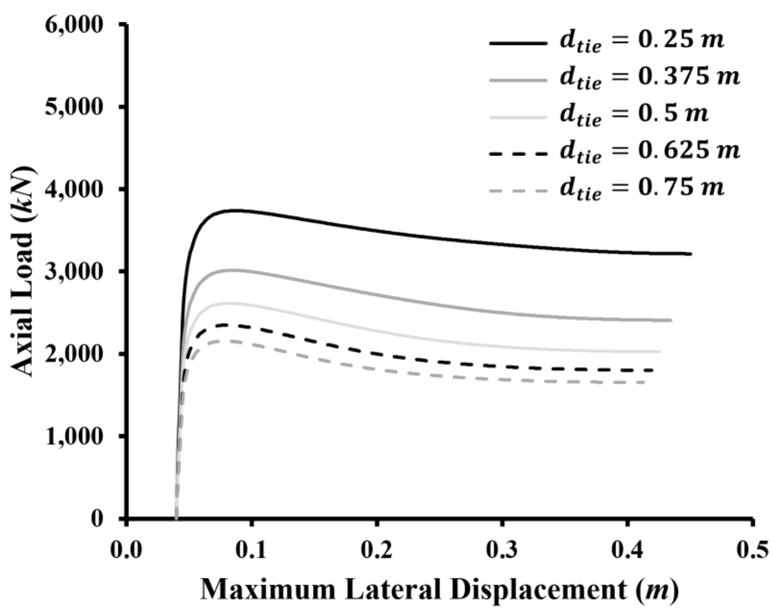

Figure 49 Maximum lateral displacement vs. applied axial load with various tie-spacing values applied to a typical rail structure

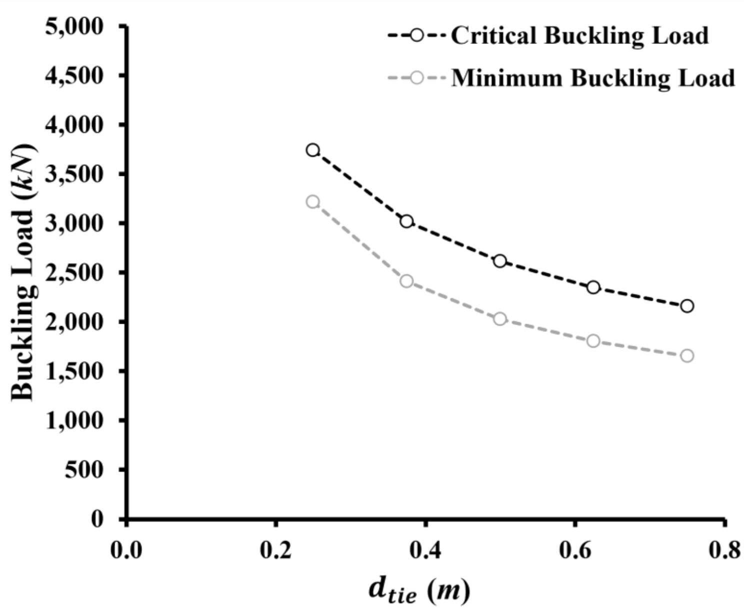

Figure 50 Predicted effect of tie-spacing value change on buckling load of a typical rail structure

These findings suggest that reducing d_{tie} in specific rail sections prone to buckling, such as areas experiencing frequent dramatic temperature changes, could be a viable strategy to mitigate buckling risks.

Sensitivity Comparison of the Rail Parameters

The effects of several key rail buckling factors, including misalignment (d_{mis}), the limit lateral tie-ballast resistance ($F_{y,lt}$), the rotational stiffness (S), the bottom friction coefficient (μ), and tie-spacing (d_{tie}), were analyzed relative to a base case under the disturbed ballast condition. The results are plotted in Figure 51.

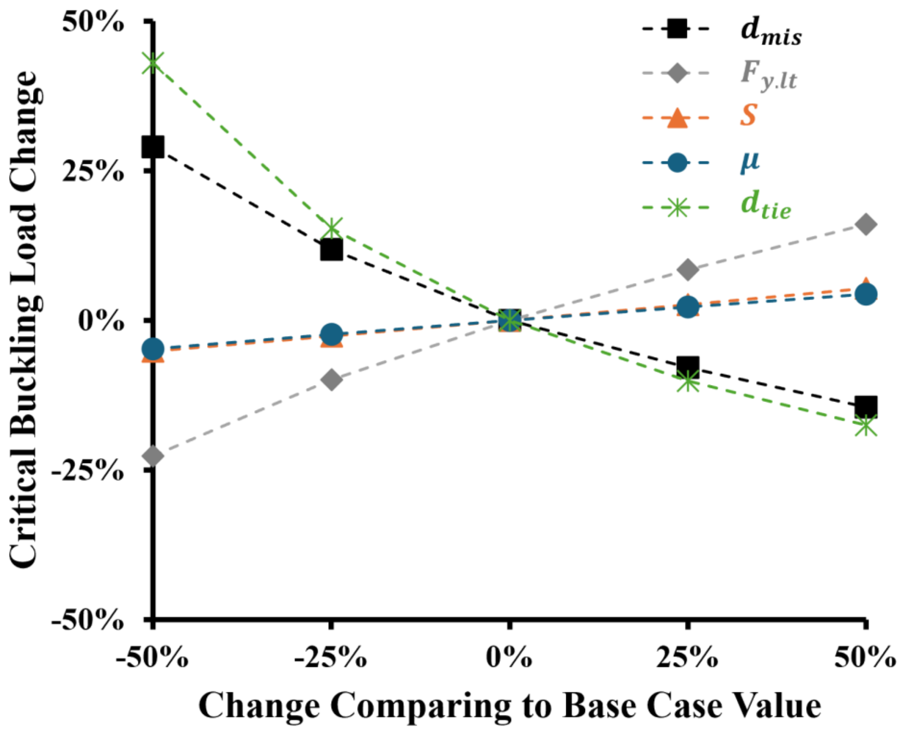

Figure 51 Sensitivity analysis showing the percentage change in critical buckling load for various rail parameters compared to their base case values

The results indicate that P_{cr} is most sensitive to d_{tie}, with a 43% variation in P_{cr} between the highest and lowest values within the tested range. However, modifying d_{tie} in existing tracks is often impractical. Among the other factors, d_{mis} demonstrates the next highest sensitivity, followed by the $F_{y,lt}$. Both of these factors have shown substantial influence on P_{cr} within the simulation range and should therefore be prioritized in rail buckling mitigation strategies.

CHAPTER V

CONCLUSION

Herein, a robust nonlinear finite element model for predicting rail buckling has been developed. By incorporating the displacement-control algorithm, the model enables post-buckling analysis to determine both the critical and minimum buckling loads. Sensitivity studies have been conducted to evaluate various parameters, demonstrating the applicability of experimental results to the model. The findings highlight that rail misalignment plays a critical role in rail buckling, emphasizing the importance of addressing even small initial imperfections to prevent derailments caused by buckling. Additionally, the lateral tie-ballast resistance significantly influences the buckling load, with the ballast condition emerging as a key factor in determining rail stability.

For future research, further sensitivity studies can be conducted if additional experimental data becomes available. Areas of interest include the effects of nonlinear fastener rotational stiffness and the friction coefficient of the tie-ballast interface. These investigations could provide deeper insights and enhance the model's predictive capabilities.

REFERENCES

Allen, D. H., & Fry, G. D. (2016). *Analysis of a Rail Subjected to Mechanical and Thermal Loading.* Report.

Allen, D. H., & Fry, G. D. (2016). *Finite Element Formulation for Thermal Buckling of Rails.* Report.

Allen, D. H., & Fry, G. D. (2017). *Finite Element Formulation and Verification for Thermal Buckling of Rail Structures in the Horizontal Plane.* Report.

Allen, D. H., & Haisler, W. E. (1985). Introduction to aerospace structural analysis. *(No Title)*.

Braun, S. (2002, July 30). *Passenger Train Cars Plunge Off Overheated Tracks.* Retrieved from Los Angeles Times: https://www.latimes.com/archives/la-xpm-2002-jul-30-na-train30-story.html

Dong, R. G., Sankar, S., & Dukkipati, R. V. (1994). A finite element model of railway track and its application to the wheel flat problem. *Proceedings of the Institution of Mechanical Engineers, Part F: Journal of Rail and Rapid Transit, 208*, 61–72.

Euler, L. (1744). *Methodus inveniendi Lineas Curvas.*

Federal Railroad Administration, O. o. (2024). Train Accidents and Rates. *Train Accidents and Rates, 2024*. Retrieved from https://safetydata.fra.dot.gov/officeofSafety/publicsite/Query/TrainAccidentsFYCYWithRates.aspx

Galilei, G. (1638). *Dialogues Concerning Two New Sciences.*

Grissom, G. T., & Kerr, A. D. (2006). Analysis of lateral track buckling using new frame-type equations. *International Journal of Mechanical Sciences*, *48*, 21-32. doi:https://doi.org/10.1016/j.ijmecsci.2005.09.006

Haisler, W. E., Stricklin, J. A., & Key, J. E. (1977). Displacement incrementation in non-linear structural analysis by the self-correcting method. *International Journal for Numerical Methods in Engineering, 11,* 3-10. doi:10.1002/nme.1620110103

Kerr, A. D. (1974). The stress and stability analyses of railroad tracks.

Kerr, A. D., & others. (1976). *Analysis of thermal track buckling in the lateral plane.* Tech. rep., United States. Federal Railroad Administration.

Kish, A., & Samavedam, G. (1991). Dynamic buckling of continuous welded rail track: Theory, tests, and safety concepts. *Transportation Research Record, 1289*, 23-38.

Kish, A., & Samavedam, G. (2013). *Track buckling prevention: theory, safety concepts, and applications.* Report, John A. Volpe National Transportation Systems Center (US).

Kish, A., Samavedam, G., & Jeong, D. Y. (1982). *Analysis of thermal buckling tests on US railroads.* Report, United States. Federal Railroad Administration.

Kish, A., Samavedam, G., Jeong, D. Y., & others. (1985). *Influence of vehicle induced loads on the lateral stability of CWR track.* Tech. rep., United States. Department of Transportation. Federal Railroad Administration.

Knoll, D. A., & Keyes, D. E. (2004). Jacobian-free Newton–Krylov methods: a survey of approaches and applications. *Journal of Computational Physics, 193*, 357-397.

Li, D., & Shust, W. (1997). *Investigation of Lateral Track Strength and Track Panel Shift Using AAR's Track Loading Vehicle.* Report.

Li, S.-R., & Batra, R. C. (2007). Thermal buckling and postbuckling of Euler-Bernoulli beams supported on nonlinear elastic foundations. *AIAA journal, 45*, 712–720.

Lim, N.-H., Park, N.-H., & Kang, Y.-J. (2003). Stability of continuous welded rail track. *Computers & Structures, 81*, 2219–2236.

Miri, A., Dhanasekar, M., Thambiratnam, D., Weston, B., & Chan, T. H. (2021). Analysis of buckling failure in continuously welded railway tracks. *Engineering Failure Analysis, 119*, 104989.

Musu, V. (2021). *Computational Model for Predicting Buckling in Rail Structures.* Thesis.

Musu, V. (2023). *Development of a Model for the Prediction of the Effects of Multiple Distinct Modes of Nonlinearity on Rail Buckling.* Thesis.

National Transportation Safety Board. (2003, August 5). *Derailment of Amtrak Auto Train P052-18 on the CSXT Railroad near Crescent City, Florida, April 18, 2002 (Report No. RAR-03-02).* Retrieved from https://www.ntsb.gov/investigations/AccidentReports/Reports/RAR0302.pdf

National Transportation Safety Board. (2004). *Railroad accident brief: DCA-02-MR-005.* Washington, D.C.: National Transportation Safety Board. Retrieved from https://www.ntsb.gov/investigations/AccidentReports/Reports/RAB0405.pdf

Nippon Steel Corporation. (2020). *Rails*. Retrieved from Rails: https://www.nipponsteel.com/product/catalog_download/pdf/K003en.pdf

Nobakht, S., Zakeri, J.-A., & Safizadeh, A. (2022). Investigation on longitudinal resistance of the ballasted railway track under vertical load. *Construction and Building Materials, 317*, 126074. doi:https://doi.org/10.1016/j.conbuildmat.2021.126074

Oden, J. T. (1967). *Mechanics of elastic structures.*

Pucillo, G. P. (2016). Thermal buckling and post-buckling behaviour of continuous welded rail track. *Vehicle System Dynamics, 54*, 1785–1807.

Saad, Y., & Schultz, M. H. (1986). GMRES: A Generalized Minimal Residual Algorithm for Solving Nonsymmetric Linear Systems. *SIAM Journal on Scientific and Statistical Computing, 7*, 856-869. doi:10.1137/0907058

Samavedam, G., Kanaan, A., Pietrak, J., Kish, A., Sluz, A., & others. (1995). *Wood tie track resistance charaterization and correlations study.* Tech. rep., United States. Department of Transportation. Federal Railroad Administration.

Samavedam, G., Kish, A., Purple, A., Schoengart, J., & others. (1993). *Parametric Analysis and Safety Concepts of CWR Track Buckling.* Tech. rep., United States. Federal Railroad Administration.

Stricklin, J. A., & Haisler, W. E. (1977). Formulations and solution procedures for nonlinear structural analysis. *Computers & Structures, 7*, 125-136.

Timoshenko, S. (1915). Strength of rails. *Transactions of the Institute of Ways and Communications, St. Petersburg, Russia*.

Timoshenko, S. (1927). Method of analysis of statical and dynamical stresses in rail.

Tvergaard, V., & Needleman, A. (1981). On localized thermal track buckling. *International Journal of Mechanical Sciences, 23*, 577-587.

Virtanen, P., Gommers, R., Oliphant, T. E., Haberland, M., Reddy, T., Cournapeau, D., . . . Contributors, S. 1. (2020). SciPy 1.0: Fundamental Algorithms for Scientific Computing in Python. *Nature Methods, 17*, 261–272. doi:10.1038/s41592-019-0686-2

Wilk, S. (2024, March). *Lateral Track Strength Increase during Maintenance Speed Restrictions.* Tech. rep., MxV Rail. Retrieved from https://www.mxvrail.com/technology-digest/lateral-track-strength-increase-during-maintenance-speed-restrictions/

Wilk, S., Li, D., Gao, Y., & Johnson, C. (2024). *FAST Baseline Ballast and Subgrade Characterization.* Tech. rep., MxV Rail.

Yang, G., & Bradford, M. A. (2016). Thermal-induced buckling and postbuckling analysis of continuous railway tracks. *International Journal of Solids and Structures, 97*, 637-649.

APPENDIX A

EXPANDED FORM OF THE STIFFNESS MATRIX AND THE FORCE VECTOR

Expanded Form of the Stiffness Matrix

The element stiffness matrix (K_{ij}^e) is previously defined by Equation (58):

$$K_{ij}^e = K_{Lin,ij}^e + K_{LS,ij}^e + K_{Geo,ij}^e + K_{LS,Geo,ij}^e + K_{T,ij}^e + K_{Lon,ij}^e + K_{Lat,ij}^e + K_{Bal,ij}^e + K_{Fas,ij}^e \tag{58}$$

The sub-terms of K_{ij}^e is expanded and each element is shown as follows:

$$K_{Lin,ij}^e = \int_0^{L^e} \left[EA\frac{d\xi_i}{dx}\frac{d\xi_j}{dx} + EI_{zz}\frac{d^2\eta_i}{dx^2}\frac{d^2\eta_j}{dx^2} + EI_{yy}\frac{d^2\zeta_i}{dx^2}\frac{d^2\zeta_j}{dx^2} \right] dx$$

$$= \frac{E}{L^e}\begin{bmatrix} A & 0 & 0 & 0 & 0 & -A & 0 & 0 & 0 & 0 \\ 0 & \frac{12I_{zz}}{(L^e)^2} & 0 & 0 & \frac{6I_{zz}}{L^e} & 0 & -\frac{12I_{zz}}{(L^e)^2} & 0 & 0 & \frac{6I_{zz}}{L^e} \\ 0 & 0 & \frac{12I_{yy}}{(L^e)^2} & -\frac{6I_{yy}}{L^e} & 0 & 0 & 0 & -\frac{12I_{yy}}{(L^e)^2} & -\frac{6I_{yy}}{L^e} & 0 \\ 0 & 0 & -\frac{6I_{yy}}{L^e} & 4I_{yy} & 0 & 0 & 0 & \frac{6I_{yy}}{L^e} & 2I_{yy} & 0 \\ 0 & \frac{6I_{zz}}{L^e} & 0 & 0 & 4I_{zz} & 0 & -\frac{6I_{zz}}{L^e} & 0 & 0 & 2I_{zz} \\ -A & 0 & 0 & 0 & 0 & A & 0 & 0 & 0 & 0 \\ 0 & -\frac{12I_{zz}}{(L^e)^2} & 0 & 0 & -\frac{6I_{zz}}{L^e} & 0 & \frac{12I_{zz}}{(L^e)^2} & 0 & 0 & -\frac{6I_{zz}}{L^e} \\ 0 & 0 & -\frac{12I_{yy}}{(L^e)^2} & \frac{6I_{yy}}{L^e} & 0 & 0 & 0 & \frac{12I_{yy}}{(L^e)^2} & \frac{6I_{yy}}{L^e} & 0 \\ 0 & 0 & -\frac{6I_{yy}}{L^e} & 2I_{yy} & 0 & 0 & 0 & \frac{6I_{yy}}{L^e} & 4I_{yy} & 0 \\ 0 & \frac{6I_{zz}}{L^e} & 0 & 0 & 2I_{zz} & 0 & -\frac{6I_{zz}}{L^e} & 0 & 0 & 4I_{zz} \end{bmatrix} \tag{111}$$

$$K_{LS,ij}^{e} = \int_{0}^{L^e} \left[EA \frac{d}{dx} \left(\sum_{m=1}^{10} \eta_m \, q_m^e \right) \frac{d\xi_i}{dx} \frac{d\eta_j}{dx} \right] dx =$$

$$= \left(q_2^e - q_7^e\right) \frac{EA}{10L^e} \begin{bmatrix} 0 & -\frac{12}{L^e} & 0 & 0 & -1 & 0 & \frac{12}{L^e} & 0 & 0 & -1 \\ 0 & 0 & 0 & 0 & 0 & 0 & 0 & 0 & 0 & 0 \\ 0 & 0 & 0 & 0 & 0 & 0 & 0 & 0 & 0 & 0 \\ 0 & 0 & 0 & 0 & 0 & 0 & 0 & 0 & 0 & 0 \\ 0 & 0 & 0 & 0 & 0 & 0 & 0 & 0 & 0 & 0 \\ 0 & \frac{12}{L^e} & 0 & 0 & 1 & 0 & -\frac{12}{L^e} & 0 & 0 & 1 \\ 0 & 0 & 0 & 0 & 0 & 0 & 0 & 0 & 0 & 0 \\ 0 & 0 & 0 & 0 & 0 & 0 & 0 & 0 & 0 & 0 \\ 0 & 0 & 0 & 0 & 0 & 0 & 0 & 0 & 0 & 0 \end{bmatrix}$$

$$+ \frac{EA}{10L^e} \begin{bmatrix} 0 & -\left(q_5^e + q_{10}^e\right) & 0 & 0 & -\frac{L^e}{3}\left(4q_5^e - q_{10}^e\right) & 0 & \left(q_5^e + q_{10}^e\right) & 0 & 0 & \frac{L^e}{3}\left(q_5^e - 4q_{10}^e\right) \\ 0 & 0 & 0 & 0 & 0 & 0 & 0 & 0 & 0 & 0 \\ 0 & 0 & 0 & 0 & 0 & 0 & 0 & 0 & 0 & 0 \\ 0 & 0 & 0 & 0 & 0 & 0 & 0 & 0 & 0 & 0 \\ 0 & \left(q_5^e + q_{10}^e\right) & 0 & 0 & \frac{L^e}{3}\left(4q_5^e - q_{10}^e\right) & 0 & -\left(q_5^e + q_{10}^e\right) & 0 & 0 & -\frac{L^e}{3}\left(q_5^e - 4q_{10}^e\right) \\ 0 & 0 & 0 & 0 & 0 & 0 & 0 & 0 & 0 & 0 \\ 0 & 0 & 0 & 0 & 0 & 0 & 0 & 0 & 0 & 0 \\ 0 & 0 & 0 & 0 & 0 & 0 & 0 & 0 & 0 & 0 \end{bmatrix} \tag{112}$$

$$K_{Geo,ij}^{e} = \int_{0}^{L^e} \left[EA \frac{d}{dx} \left(\sum_{m=1}^{10} \eta_m \, q_m^e \right) \frac{d\eta_i}{dx} \frac{d\xi_j}{dx} \right] dx + \int_{0}^{L^e} \left[EA \frac{d}{dx} \left(\sum_{m=1}^{10} \xi_m \, q_m^e \right) \frac{d\eta_i}{dx} \frac{d\eta_j}{dx} \right] dx$$

$$= \frac{EA}{10L^e} \begin{bmatrix} 0 & 0 & 0 & 0 & 0 & 0 & 0 & 0 & 0 & 0 \\ -\frac{12}{L^e}(q_2^e - q_7^e) - (q_5^e + q_{10}^e) & 0 & 0 & 0 & 0 & \frac{12}{L^e} * (q_2^e - q_7^e) + (q_5^e + q_{10}^e) & 0 & 0 & 0 & 0 \\ 0 & 0 & 0 & 0 & 0 & 0 & 0 & 0 & 0 & 0 \\ 0 & 0 & 0 & 0 & 0 & 0 & 0 & 0 & 0 & 0 \\ -(q_2^e - q_7^e) - \frac{L^e}{3}(4q_5^e - q_{10}^e) & 0 & 0 & 0 & 0 & (q_2^e - q_7^e) + \frac{L^e}{3} * (4q_5^e - q_{10}^e) & 0 & 0 & 0 & 0 \\ 0 & 0 & 0 & 0 & 0 & 0 & 0 & 0 & 0 & 0 \\ \frac{12}{L^e} * (q_2^e - q_7^e) + (q_5^e + q_{10}^e) & 0 & 0 & 0 & 0 & -\frac{12}{L^e} * (q_2^e - q_7^e) - (q_5^e + q_{10}^e) & 0 & 0 & 0 & 0 \\ 0 & 0 & 0 & 0 & 0 & 0 & 0 & 0 & 0 & 0 \\ 0 & 0 & 0 & 0 & 0 & 0 & 0 & 0 & 0 & 0 \\ -(q_2^e - q_7^e) + \frac{L^e}{3} * (q_5^e - 4q_{10}^e) & 0 & 0 & 0 & 0 & (q_2^e - q_7^e) - \frac{L^e}{3} * (q_5^e - 4q_{10}^e) & 0 & 0 & 0 & 0 \end{bmatrix} \tag{113}$$

$$+ (q_1^e - \ q_6^e) \frac{EA}{10L^e} \begin{bmatrix} 0 & 0 & 0 & 0 & 0 & 0 & 0 & 0 & 0 & 0 \\ 0 & -\frac{12}{L^e} & 0 & 0 & -1 & 0 & \frac{12}{L^e} & 0 & 0 & -1 \\ 0 & 0 & 0 & 0 & 0 & 0 & 0 & 0 & 0 & 0 \\ 0 & 0 & 0 & 0 & 0 & 0 & 0 & 0 & 0 & 0 \\ 0 & -1 & 0 & 0 & -\frac{4L^e}{3} & 0 & 1 & 0 & 0 & \frac{L^e}{3} \\ 0 & 0 & 0 & 0 & 0 & 0 & 0 & 0 & 0 & 0 \\ 0 & \frac{12}{L^e} & 0 & 0 & 1 & 0 & -\frac{12}{L^e} & 0 & 0 & 1 \\ 0 & 0 & 0 & 0 & 0 & 0 & 0 & 0 & 0 & 0 \\ 0 & 0 & 0 & 0 & 0 & 0 & 0 & 0 & 0 & 0 \\ 0 & -1 & 0 & 0 & \frac{L^e}{3} & 0 & 1 & 0 & 0 & -\frac{4L^e}{3} \end{bmatrix}$$

$$K^{e}_{LS,Geo,ij} = \int_0^{L^e} \left[\frac{3EA}{2}\frac{d}{dx}\left(\sum_{m=1}^{10}\eta_m\, q^e_m\right)\frac{d}{dx}\left(\sum_{n=1}^{10}\eta_n\, q^e_n\right)\frac{d\eta_i}{dx}\frac{d\eta_j}{dx}\right]dx$$

$$= \begin{bmatrix} 0 & 0 & 0 & 0 & 0 & 0 & 0 & 0 & 0 & 0 \\ 0 & c_{2,2} & 0 & 0 & c_{2,5} & 0 & c_{2,7} & 0 & 0 & c_{2,10} \\ 0 & 0 & 0 & 0 & 0 & 0 & 0 & 0 & 0 & 0 \\ 0 & 0 & 0 & 0 & 0 & 0 & 0 & 0 & 0 & 0 \\ 0 & c_{5,2} & 0 & 0 & c_{5,5} & 0 & c_{5,7} & 0 & 0 & c_{5,10} \\ 0 & 0 & 0 & 0 & 0 & 0 & 0 & 0 & 0 & 0 \\ 0 & c_{7,2} & 0 & 0 & c_{7,5} & 0 & c_{7,7} & 0 & 0 & c_{7,10} \\ 0 & 0 & 0 & 0 & 0 & 0 & 0 & 0 & 0 & 0 \\ 0 & 0 & 0 & 0 & 0 & 0 & 0 & 0 & 0 & 0 \\ 0 & c_{10,2} & 0 & 0 & c_{10,5} & 0 & c_{10,7} & 0 & 0 & c_{10,10} \end{bmatrix} \tag{114}$$

Here:

$$c_{2,2} = c_{7,7} = \frac{9EA}{70(L^e)^3}[((q^e_5)^2 + (q^e_{10})^2)(L^e)^2 + 6(q^e_5 + q^e_{10})(q^e_2 - q^e_7)L^e + 24(q^e_2 - q^e_7)^2] \tag{115}$$

$$c_{2,5} = c_{5,2} = \frac{3EA}{280}\left[\frac{36(q^e_2 - q^e_7)^2}{(L^e)^2} + \frac{24q^e_5(q^e_2 - q^e_7)}{L^e} + (q^e_5 + q^e_{10})^2 - 2(q^e_5)^2\right] \tag{116}$$

$$c_{2,7} = c_{7,2} = -\frac{9EA}{70(L^e)^3}[((q^e_5)^2 + (q^e_{10})^2)(L^e)^2 + 6(q^e_5 + q^e_{10})(q^e_2 - q^e_7)L^e + 24(q^e_2 - q^e_7)^2] \tag{117}$$

$$c_{2,10} = c_{10,2} = \frac{3EA}{280}\left[\frac{36(q^e_2 - q^e_7)^2}{(L^e)^2} + \frac{24q^e_{10}(q^e_2 - q^e_7)}{L^e} + (q^e_5 + q^e_{10})^2 - 2(q^e_{10})^2\right] \tag{118}$$

$$c_{5,5} = \frac{EA}{140}\left[\frac{18(q_2^e - q_7^e)^2}{L^e} - 3(q_2^e - q_7^e)(q_5^e - q_{10}^e) \right.$$

$$\left. + (12(q_5^e)^2 - 3q_5^e q_{10}^e + (q_{10}^e)^2)L^e \right] \tag{119}$$

$$c_{5,7} = c_{7,5} = -\frac{3EA}{280}\left[\frac{36(q_2^e - q_7^e)^2}{(L^e)^2} + \frac{24q_5^e(q_2^e - q_7^e)}{L^e} + (q_5^e + q_{10}^e)^2 - 2(q_5^e)^2\right] \tag{120}$$

$$c_{5,10} = c_{10,5} = \frac{EA}{280}[6(q_2^e - q_7^e)(q_5^e + q_{10}^e) - 3((q_5^e)^2 + (q_{10}^e)^2)L^e + 4q_5^e q_{10}^e L^e] \tag{121}$$

$$c_{7,10} = c_{10,7} = -\frac{3EA}{280}\left[\frac{36(q_2^e - q_7^e)^2}{(L^e)^2} + \frac{24q_{10}^e(q_2^e - q_7^e)}{L^e} + (q_5^e + q_{10}^e)^2 - 2(q_{10}^e)^2\right] \tag{122}$$

$$c_{10,10} = \frac{EA}{140}\left[\frac{18(q_2^e - q_7^e)^2}{L^e} + 3(q_2^e - q_7^e)(q_5^e - q_{10}^e) \right.$$

$$\left. + ((q_5^e)^2 - 3q_5^e q_{10}^e + 12(q_{10}^e)^2)L^e \right] \tag{123}$$

$$K_{T,i}^{e} = -\int_{0}^{L^{e}} \left[P^{T} \frac{d\eta_i}{dx} \frac{d\eta_j}{dx} \right] dx$$

$$= -P^{T} \begin{bmatrix} 0 & 0 & 0 & 0 & 0 & 0 & 0 & 0 & 0 & 0 \\ 0 & \frac{6}{5L^{e}} & 0 & 0 & \frac{1}{10} & 0 & -\frac{6}{5L^{e}} & 0 & 0 & \frac{1}{10} \\ 0 & 0 & 0 & 0 & 0 & 0 & 0 & 0 & 0 & 0 \\ 0 & 0 & 0 & 0 & 0 & 0 & 0 & 0 & 0 & 0 \\ 0 & \frac{1}{10} & 0 & 0 & \frac{2L^{e}}{15} & 0 & -\frac{1}{10} & 0 & 0 & -\frac{L^{e}}{30} \\ 0 & 0 & 0 & 0 & 0 & 0 & 0 & 0 & 0 & 0 \\ 0 & -\frac{6}{5L^{e}} & 0 & 0 & -\frac{1}{10} & 0 & \frac{6}{5L^{e}} & 0 & 0 & -\frac{1}{10} \\ 0 & 0 & 0 & 0 & 0 & 0 & 0 & 0 & 0 & 0 \\ 0 & 0 & 0 & 0 & 0 & 0 & 0 & 0 & 0 & 0 \\ 0 & \frac{1}{10} & 0 & 0 & -\frac{L^{e}}{30} & 0 & -\frac{1}{10} & 0 & 0 & \frac{2L^{e}}{15} \end{bmatrix} \tag{124}$$

$$K_{Lon,i}^{e} = -\int_{0}^{L^e} \xi_i \frac{\partial f_x}{\partial q_j^e}\, dx - \int_{0}^{L^e} z^* \frac{d\zeta_i}{dx} \frac{\partial f_x}{\partial q_j^e}\, dx$$

$$= \frac{\lambda_x \cdot k_x}{d_{tie}} \cdot \left[\int_{0}^{L^e} \xi_i\, \xi_j\, dx + \int_{0}^{L^e} z^* \frac{d\zeta_i}{dx}\, \xi_j\, dx \right]$$

$$= \frac{\lambda_x\, k_x}{d_{tie}} \begin{bmatrix} \frac{L^e}{3} & 0 & 0 & 0 & 0 & \frac{L^e}{6} & 0 & 0 & 0 & 0 \\ 0 & 0 & 0 & 0 & 0 & 0 & 0 & 0 & 0 & 0 \\ 0 & 0 & 0 & 0 & 0 & 0 & 0 & 0 & 0 & 0 \\ 0 & 0 & 0 & 0 & 0 & 0 & 0 & 0 & 0 & 0 \\ 0 & 0 & 0 & 0 & 0 & 0 & 0 & 0 & 0 & 0 \\ \frac{L^e}{6} & 0 & 0 & 0 & 0 & \frac{L^e}{3} & 0 & 0 & 0 & 0 \\ 0 & 0 & 0 & 0 & 0 & 0 & 0 & 0 & 0 & 0 \\ 0 & 0 & 0 & 0 & 0 & 0 & 0 & 0 & 0 & 0 \\ 0 & 0 & 0 & 0 & 0 & 0 & 0 & 0 & 0 & 0 \\ 0 & 0 & 0 & 0 & 0 & 0 & 0 & 0 & 0 & 0 \end{bmatrix} \qquad (125)$$

$$+ \frac{\lambda_x\, k_x\, z^*}{d_{tie}} \begin{bmatrix} 0 & 0 & 0 & 0 & 0 & 0 & 0 & 0 & 0 & 0 \\ 0 & 0 & 0 & 0 & 0 & 0 & 0 & 0 & 0 & 0 \\ -\frac{1}{2} & 0 & 0 & 0 & 0 & -\frac{1}{2} & 0 & 0 & 0 & 0 \\ -\frac{L^e}{12} & 0 & 0 & 0 & 0 & \frac{L^e}{12} & 0 & 0 & 0 & 0 \\ 0 & 0 & 0 & 0 & 0 & 0 & 0 & 0 & 0 & 0 \\ 0 & 0 & 0 & 0 & 0 & 0 & 0 & 0 & 0 & 0 \\ 0 & 0 & 0 & 0 & 0 & 0 & 0 & 0 & 0 & 0 \\ \frac{1}{2} & 0 & 0 & 0 & 0 & \frac{1}{2} & 0 & 0 & 0 & 0 \\ \frac{L^e}{12} & 0 & 0 & 0 & 0 & -\frac{L^e}{12} & 0 & 0 & 0 & 0 \\ 0 & 0 & 0 & 0 & 0 & 0 & 0 & 0 & 0 & 0 \end{bmatrix}$$

$$K_{Lat,i}^{e} = -\int_0^{L^e} \eta_i \frac{\partial f_y}{\partial q_j^e}\, dx = \frac{\lambda_y \cdot k_{y,1}}{d_{tie}} \int_0^{L_1^e} \eta_i \eta_j \, dx + \frac{\lambda_y \cdot k_{y,2}}{d_{tie}} \int_0^{L_2^e} \eta_i \eta_j \, dx$$

$$= \frac{\lambda_y}{d_{tie}} \frac{F_{y,pk}}{v_{pk}} \begin{bmatrix} 0 & 0 & 0 & 0 & 0 & 0 & 0 & 0 & 0 & 0 \\ 0 & \frac{13L_1^e}{35} & 0 & 0 & \frac{11(L_1^e)^2}{210} & 0 & \frac{9L_1^e}{70} & 0 & 0 & -\frac{13(L_1^e)^2}{420} \\ 0 & 0 & 0 & 0 & 0 & 0 & 0 & 0 & 0 & 0 \\ 0 & 0 & 0 & 0 & 0 & 0 & 0 & 0 & 0 & 0 \\ 0 & \frac{11(L_1^e)^2}{210} & 0 & 0 & \frac{(L_1^e)^3}{105} & 0 & \frac{13(L_1^e)^2}{420} & 0 & 0 & -\frac{(L_1^e)^3}{140} \\ 0 & 0 & 0 & 0 & 0 & 0 & 0 & 0 & 0 & 0 \\ 0 & \frac{9L_1^e}{70} & 0 & 0 & \frac{13(L_1^e)^2}{420} & 0 & \frac{13L_1^e}{35} & 0 & 0 & -\frac{11(L_1^e)^2}{210} \\ 0 & 0 & 0 & 0 & 0 & 0 & 0 & 0 & 0 & 0 \\ 0 & 0 & 0 & 0 & 0 & 0 & 0 & 0 & 0 & 0 \\ 0 & -\frac{13(L_1^e)^2}{420} & 0 & 0 & -\frac{(L_1^e)^3}{140} & 0 & -\frac{11(L_1^e)^2}{210} & 0 & 0 & \frac{(L_1^e)^3}{105} \end{bmatrix} \tag{126}$$

$$+ \frac{\lambda_y}{d_{tie}} \frac{F_{y,lt} - F_{y,pk}}{v_{lt} - v_{pk}} \begin{bmatrix} 0 & 0 & 0 & 0 & 0 & 0 & 0 & 0 & 0 & 0 \\ 0 & \frac{13L_2^e}{35} & 0 & 0 & \frac{11(L_2^e)^2}{210} & 0 & \frac{9L_2^e}{70} & 0 & 0 & -\frac{13(L_2^e)^2}{420} \\ 0 & 0 & 0 & 0 & 0 & 0 & 0 & 0 & 0 & 0 \\ 0 & 0 & 0 & 0 & 0 & 0 & 0 & 0 & 0 & 0 \\ 0 & \frac{11(L_2^e)^2}{210} & 0 & 0 & \frac{(L_2^e)^3}{105} & 0 & \frac{13(L_2^e)^2}{420} & 0 & 0 & -\frac{(L_2^e)^3}{140} \\ 0 & 0 & 0 & 0 & 0 & 0 & 0 & 0 & 0 & 0 \\ 0 & \frac{9L_2^e}{70} & 0 & 0 & \frac{13(L_2^e)^2}{420} & 0 & \frac{13L_2^e}{35} & 0 & 0 & -\frac{11(L_2^e)^2}{210} \\ 0 & 0 & 0 & 0 & 0 & 0 & 0 & 0 & 0 & 0 \\ 0 & 0 & 0 & 0 & 0 & 0 & 0 & 0 & 0 & 0 \\ 0 & -\frac{13(L_2^e)^2}{420} & 0 & 0 & -\frac{(L_2^e)^3}{140} & 0 & -\frac{11(L_2^e)^2}{210} & 0 & 0 & \frac{(L_2^e)^3}{105} \end{bmatrix}$$

(Note that here, the trilinear formulation for lateral tie-ballast resistance is employed for $K_{Lat,i}^{e}$)

$$K^e_{Bal,i} = -\int_0^{L^e} \zeta_i \frac{\partial f_z}{\partial q^e_j}\, dx = \frac{k_z}{d_{tie}} \int_0^{L^e} \zeta_i \zeta_j\, dx$$

$$= \frac{k_z}{d_{tie}} \begin{bmatrix} 0 & 0 & 0 & 0 & 0 & 0 & 0 & 0 & 0 & 0 \\ 0 & 0 & 0 & 0 & 0 & 0 & 0 & 0 & 0 & 0 \\ 0 & 0 & \frac{13L^e}{35} & -\frac{11(L^e)^2}{210} & 0 & 0 & 0 & \frac{9L^e}{70} & \frac{13(L^e)^2}{420} & 0 \\ 0 & 0 & -\frac{11(L^e)^2}{210} & \frac{(L^e)^3}{105} & 0 & 0 & 0 & -\frac{13(L^e)^2}{420} & -\frac{(L^e)^3}{140} & 0 \\ 0 & 0 & 0 & 0 & 0 & 0 & 0 & 0 & 0 & 0 \\ 0 & 0 & 0 & 0 & 0 & 0 & 0 & 0 & 0 & 0 \\ 0 & 0 & 0 & 0 & 0 & 0 & 0 & 0 & 0 & 0 \\ 0 & 0 & \frac{9L^e}{70} & -\frac{13(L^e)^2}{420} & 0 & 0 & 0 & \frac{13L^e}{35} & \frac{11(L^e)^2}{210} & 0 \\ 0 & 0 & \frac{13(L^e)^2}{420} & -\frac{(L^e)^3}{140} & 0 & 0 & 0 & \frac{11(L^e)^2}{210} & \frac{(L^e)^3}{105} & 0 \\ 0 & 0 & 0 & 0 & 0 & 0 & 0 & 0 & 0 & 0 \end{bmatrix} \tag{127}$$

$$K^e_{Fas,i} = -\int_0^{L^e} \frac{d\eta_i}{dx} \frac{\partial \tau_z}{\partial q^e_j}\, dx = \frac{S}{d_{tie}} \int_0^{L^e} \frac{d\eta_i}{dx} \frac{d\eta_j}{dx}\, dx$$

$$= \frac{S}{d_{tie}} \begin{bmatrix} 0 & 0 & 0 & 0 & 0 & 0 & 0 & 0 & 0 & 0 \\ 0 & \frac{6}{5L^e} & 0 & 0 & \frac{1}{10} & 0 & -\frac{6}{5L^e} & 0 & 0 & \frac{1}{10} \\ 0 & 0 & 0 & 0 & 0 & 0 & 0 & 0 & 0 & 0 \\ 0 & 0 & 0 & 0 & 0 & 0 & 0 & 0 & 0 & 0 \\ 0 & \frac{1}{10} & 0 & 0 & \frac{2L^e}{15} & 0 & -\frac{1}{10} & 0 & 0 & -\frac{L^e}{30} \\ 0 & 0 & 0 & 0 & 0 & 0 & 0 & 0 & 0 & 0 \\ 0 & -\frac{6}{5L^e} & 0 & 0 & -\frac{1}{10} & 0 & \frac{6}{5L^e} & 0 & 0 & -\frac{1}{10} \\ 0 & 0 & 0 & 0 & 0 & 0 & 0 & 0 & 0 & 0 \\ 0 & 0 & 0 & 0 & 0 & 0 & 0 & 0 & 0 & 0 \\ 0 & \frac{1}{10} & 0 & 0 & -\frac{L^e}{30} & 0 & -\frac{1}{10} & 0 & 0 & \frac{2L^e}{15} \end{bmatrix} \tag{128}$$

Expanded Form of the Force Vector

The external distributed load is assumed to vary linearly within the element, and the superscripts 0 and L of p_x, p_y, and p_z indicate the corresponding load values at $x = 0$ and $x = L$, respectively:

$$p_x = p_x^0 + \left(\frac{x}{L}\right)(p_x^L - p_x^0) \tag{129}$$

$$p_y = p_y^0 + \left(\frac{x}{L}\right)(p_y^L - p_y^0) \tag{130}$$

$$p_z = p_z^0 + \left(\frac{x}{L}\right)(p_z^L - p_z^0) \tag{131}$$

These values should be defined a priori as boundary conditions.

The force vector (F_i^e) due to external distributive loads (p_x, p_y, p_z), is expanded as:

$$F_i^e = \int_0^{L^e} \left[p_x \xi_i + p_y \eta_i + p_z \zeta_i + P^T \frac{d\xi_i}{dx} \right] dx = \begin{bmatrix} \frac{L^e(2p_x^0 + p_x^L)}{6} - EA\alpha\Delta T \\ \frac{L^e\left(7p_y^0 + 3p_y^L\right)}{20} \\ \frac{L^e(7p_z^0 + 3p_z^L)}{20} \\ -\frac{(L^e)^2(3p_z^0 + 2p_z^L)}{60} \\ \frac{(L^e)^2\left(3p_y^0 + 2p_y^L\right)}{60} \\ \frac{L^e(p_x^0 + 2p_x^L)}{6} + EA\alpha\Delta T \\ \frac{L^e\left(3p_y^0 + 7p_y^L\right)}{20} \\ \frac{L^e(3p_z^0 + 7p_z^L)}{20} \\ \frac{(L^e)^2(2p_z^0 + 3p_z^L)}{60} \\ -\frac{(L^e)^2\left(2p_y^0 + 3p_y^L\right)}{60} \end{bmatrix} \tag{132}$$

In addition, any external concentrated force or moment should be added directly to the force vector, ensuring that it corresponds to the appropriate degrees of freedom.

APPENDIX B

UNIT CONVERSION

The following tables provide the necessary multiplication factors for converting between commonly used units of force, length, pressure, and thermal expansion coefficients:

Table 4 Multiplication factors for force unit conversion (3 significant digits)

From \ To	***N***	***kN***	***lbf***	***kips***
N **(Newton)**	1.00	0.00100	0.225	0.000225
kN **(Kilonewton)**	1000	1.00	225	0.225
lbf **(Pound)**	4.45	0.00445	1.00	0.00100
kips **(kilo-pound)**	4450	4.45	1000	1.00

Table 5 Multiplication factors for length unit conversion (3 significant digits)

From \ To	***m***	***mm***	***cm***	***in***	***ft***
m **(meter)**	1.00	1000	100	39.4	3.28
mm **(millimeter)**	0.00100	1.00	0.100	0.0394	0.00328
cm **(centimeter)**	0.0100	10.0	1.00	0.394	0.0328
in **(inch)**	0.0254	25.4	2.54	1.00	0.0833
ft **(foot)**	0.305	305	30.5	12.0	1.00

Table 6 Multiplication factors for pressure unit conversion (3 significant digits)

From \ To	***Pa***	***psi***
***Pa* (Pascal)**	1.00	0.000145
***psi* (pounds per square inch)**	6900	1.00

Table 7 Multiplication Factors for thermal expansion coefficient unit conversion (3 significant digits)

From \ To	**1/$^o C$**	**1/$^o F$**
1/$^o C$	1.00	0.556
1/$^o F$	1.80	1.00